University of Alberta

Supercontinuum Probe of Ultrafast Carrier Dynamics in Nanostructured Silicon Thin Films

By

Rahma Al Harthy

A thesis submitted to the Faculty of Graduate Studies and Research in Partial Fulfillment of the requirements for the degree of Master of Science

Department of Physics

Edmonton, Alberta

Spring 2008

Library and Archives Canada

Published Heritage Branch

395 Wellington Street
Ottawa ON K1A 0N4
Canada

Bibliothèque et Archives Canada

Direction du Patrimoine de l'édition

395, rue Wellington
Ottawa ON K1A 0N4
Canada

Your file Votre référence
ISBN: 978-0-494-45770-2
Our file Notre référence
ISBN: 978-0-494-45770-2

NOTICE:
The author has granted a non-exclusive license allowing Library and Archives Canada to reproduce, publish, archive, preserve, conserve, communicate to the public by telecommunication or on the Internet, loan, distribute and sell theses worldwide, for commercial or non-commercial purposes, in microform, paper, electronic and/or any other formats.

The author retains copyright ownership and moral rights in this thesis. Neither the thesis nor substantial extracts from it may be printed or otherwise reproduced without the author's permission.

AVIS:
L'auteur a accordé une licence non exclusive permettant à la Bibliothèque et Archives Canada de reproduire, publier, archiver, sauvegarder, conserver, transmettre au public par télécommunication ou par l'Internet, prêter, distribuer et vendre des thèses partout dans le monde, à des fins commerciales ou autres, sur support microforme, papier, électronique et/ou autres formats.

L'auteur conserve la propriété du droit d'auteur et des droits moraux qui protège cette thèse. Ni la thèse ni des extraits substantiels de celle-ci ne doivent être imprimés ou autrement reproduits sans son autorisation.

In compliance with the Canadian Privacy Act some supporting forms may have been removed from this thesis.

While these forms may be included in the document page count, their removal does not represent any loss of content from the thesis.

Conformément à la loi canadienne sur la protection de la vie privée, quelques formulaires secondaires ont été enlevés de cette thèse.

Bien que ces formulaires aient inclus dans la pagination, il n'y aura aucun contenu manquant.

Canada

Abstract

An optical pump-supercontinuum-probe (PSCP) setup for transient absorption measurements was developed and extensively characterized using an optical Kerr gate (OKG). The time resolution of the setup is in the order of hundreds of femtoseconds, and the available probe wavelength range extends from 450 nm to 700 nm. This PSCP setup was used to probe ultrafast carrier dynamics in various nanostructured silicon thin films, which included amorphous, polycrystalline and silicon nanocrystal films. The samples varied in deposition method, annealing temperature, and thickness. The influence of these sample fabrication parameters, as well as the pump fluence and the probe wavelength, on the photoexcited carrier dynamics was investigated. Complementary studies of these samples were undertaken using photoluminescence and steady-state optical transmission techniques. The observed relaxation mechanisms are discussed. The transient photoinduced absorption in the silicon nanocrystal film revealed the presence of two different relaxation mechanisms. A fast relaxation with a decay time ranging from (0.52 ± 0.09) ps at a probe wavelength of 600 nm to a pulse-width-limited relaxation time at a probe wavelength of 700 nm was attributed to relaxation of carriers to interface states. A slow relaxation process with a decay time decreasing from (6.1 ± 0.9) ps for 600 nm probe to (4.8 ± 0.3) ps for 700 nm probe corresponds to the relaxation of the carriers within the nanocrystals.

Acknowledgments

First of all, I thank God almighty, who in His infinite greatness, sublimeness, magnanimity and kindness made the accomplishment of this degree possible.

Moreover, I would like to acknowledge and extend my heartfelt gratitude to the following people, who have helped me in the completion of this thesis:

My supervisor, Dr. Frank Hegmann for his vital supervision, understanding, assistance and support.

Dr. Al Meldrum for opening his labs for us for the synthesis of samples, measuring the photoluminescence and transmission spectra.

Dr. Sulan Kuai for kindly synthesizing and characterizing our samples.

Dr. Lyubov Titova for reviewing and editing this thesis and supplying useful comments and suggestions on thesis writing.

Dr. Amena Khan for her dual assistance in both thesis writing and living matters in Edmonton.

Tony Walford for making the brilliant sample holder that was brand new to the lab and will be useful for many samples in the future as well.

Dr. Aaron Slepkov for introducing me to the ultrafast spectroscopy lab and particularly the supercontinuum generation.

Jianbo Gao, for providing technical help with the laser system in the lab.

Sultan Qaboos University, for providing me with the scholarship and opportunity to continue my study abroad.

My cousin Wafa Al Harthy, her husband Saif Al Zaaby and their lovely daughter Mayce, for being my family in Edmonton and making my experience abroad easier and smoother.

My family, for the encouragement and support.

And finally, my husband Ahmed Al Harthy for his continuous and remote support and encouragement all the time despite the thousands miles between us.

Contents

1 Introduction.....1

1.1 Motivation for Studying Ultrafast Carrier Dynamics in Silicon Nanostructures....1
1.2 Ultrafast Carrier Dynamics in Semiconductors.....2
1.3 Pump-Probe Technique.....5
1.4 Previous Work.....12

2 Propagation and Measurement of Ultrashort Pulses.....14

2.1 Ultrashort Laser Pulses.....14
2.2 Propagation of Short Pulses in the Linear Optics Regime.....15
2.3 Propagation of Short Laser Pulses in the Nonlinear Regime.....17
2.4 Supercontinuum Generation.....20
2.5 Measurements of Ultrashort Pulses.....21

3 The PSCP Setup and Methodology.....25

3.1 Experimental Layout.....25
3.2 Data Acquisition and Experimental Considerations.....29

3.2.1 Pump and Probe beams Spatial Profile.....29
3.2.2 Determination of Zero Time Delay t_0.....31
3.2.3 Linearity of Detectors.....32
3.2.4 Detectors Responsivity.....33

4 Characterization of the Experimental Setup.....38

4.1 Second Harmonic Generation.....38
4.2 Supercontinuum Characterization.....39
4.3 Pulse Characterization.....44

4.3.1 Temporal Resolution.....44

4.3.1.1 Angle Between Pump and Probe Beams.....44
4.3.1.2 Pulse Compressor Settings.....45

4.3.2 Temporal Broadening.....46
4.3.3 Chirp.....51

5 The Study of Nanostructured Silicon Thin Films.....52

5.1 Silicon Thin Films.....52

5.1.1 Sample Preparation.....52
5.1.2 Transmission Spectra.....53
5.1.3 Ultrafast Carrier Dynamics.....55

5.1.3.1 Effect of Annealing.....55
5.1.3.2 Thickness Dependence.....57
5.1.3.3 Probe Wavelength Dependence.....60
5.1.3.4 Pump Fluence Dependence.....61

5.2 Silicon Nanocrystal Thin Film.....64

5.2.1 Sample Preparation.....64
5.2.2 Ultrafast Carrier Dynamics in Si Nanocrystal Film.....65

5.2.2.1 Probe Wavelength Dependence.....65
5.2.2.2 Pump Fluence Dependence.....67

6 Conclusions and Future Directions.....69

Appendix A.....72

A.1 Pulse Broadening and Relative Arrival Time Calculations.....72

Appendix B.....75

B.1 Experiment Consistency.....75
B.2 Probe Fluence Dependence.....76
B.3 Residual Signal.....77
B.4 Stimulated Emission Check.....78

References.....80

List of Tables

Table 4.1: Values of the FWHM of different pump probe cross correlation signal, the corresponding decorrelation factor γ, the corresponding probe pulse duration, Δt, and the pulse duration-bandwidth product obtained for the duration of the probe pulses at different wavelengths.....49

Table A.1: Dispersion relation and thicknesses for different optical elements between water cell and sample.....72

Table A.2. Values used to calculate temporal broadening and relative arrival time.....73

List of Figures

Figure 1.1: Photoexcitation and relaxation of carriers in bulk semiconductors. (1) Excitation of electrons to the conduction band. (2) Relaxation of electrons to the conduction band edge and holes to the valence band edge (3) Recombination of electrons in the conduction band with holes in the valence band.....3

Figure 1.2. Phoexcitation and relaxation of semiconductor nanocrystals. (1) Excitation of electrons to the conduction band. (2) Relaxation of electrons to the conduction band edge and holes to the valence band edge. (3) Trapping of carriers in the interface states (4) Recombination of electrons in the interface states with holes in the valence band. (Adapted from Pavesi *et al.*, 2000).....4

Figure 1.3: Auger process. (Adapted from Pavesi, 2006).....5

Figure 1.4: Schematic diagram of the pump-probe technique.....6

Figure 1.5: Time evolution of the transient transmission or reflection signal in a pump probe experiment. (Adapted from Andor technology catalogue).....6

Figure 1.6: (a) Bleaching of interband transitions by pump pulse. (b) The corresponding transient absorption signal with initial decrease in absorption of the probe beam.....10

Figure 1.7: (a) Absorption of the probe pulse by the free photoexcited carriers and by carriers trapped in the interface states. (b) The corresponding transient absorption signal with initial increase in the absorption of probe beam.....11

Figure 2.1: Self phase modulation. (Adapted from Steinmeyer *et al.*, 1999).....19

Figure 2.2: Self-focusing of ultrashort pulse. (Adapted from Antoncini) 19

Figure 2.3: Optical Kerr Gate. (Adapted from Slepkov, 2002).....22

Figure 2.4: The decorrelation factor γ for $sech^2$ (1) and Gaussian (2) as a function of the normalized pump pulse duration to the FWHM duration of the correlation function (Adapted from Albrecht et al.1992).....24

Figure 3.1: The PSCP setup. All optics are optimized for the corresponding wavelengths. $\lambda/2$: half wave plate, P_1,P_2:Polarizers, P_3: broadband Glan-laser polarizer, L_1=20cm lens, L_2=30cm lens, L_3=-10cm lens, L_4=7.5cm achromat doublet lens, L_5,L_6,L_7,L_8=10cm achromat doublet lenses. BP: Band Pass filter. ND: neutral density filter. PC: personal computer.....26

Figure 3.2: The optical Kerr Gate Setup for the zero time delay measurement.....27

Figure 3.3: The optical Kerr Gate Setup for pulse characterization.....28

Figure 3.4: Spatial profiles of the pump and probe beams at the sample position.....30

Figure 3.5: Transient absorption signal and pump probe correlation signal obtained by Kerr gate.....31

Figure 3.6: Linearity of detector A (a) and detector B (b).....32

Figure 3.7: Resposivity of the detectors as a function of the wavelength.....33

Figure 3.8: Example of the experimental data. Traces A and B are shifted for clarity. Signals A and B were detected with the sensitivity of the lock-ins set to 5 mV, while the sensitivity of the third lock-in monitoring the signal A – B was 50 μV.....34

Figure 3.9: (a) The absolute data A/B (b) the differential data (A-B)/B as a function of the delay time (c) The calibrated data $-\Delta T/T_0$. This data is the average of three scans.....36

Figure 4.1: The 400 nm pump beam spectrum. Inset: squares – experimental points, curve – Gaussian fit of FWHM of (3.9 ± 0.1) nm.....39

Figure 4.2: SC spectra at different generating powers on a linear-linear scale (a) and on a log-linear scale (b).....41

Figure 4.3: (a) SC power at different positions in the experimental setup. Each data point represents the power within 10 nm bandwidth around each probe wavelength as selected by BP filter. (b) Transmission through the 435 nm long pass filter (Thorlabs Catalogue). (c) Transmission through the IR cutoff filter (Edmund Catalogue).....43

Figure 4.4: The pump-probe cross correlation signal dependence on the angle between the pump and probe beams. The FWHM at angle smaller than 10^0 is equal to (0.338 ± 0.001) ps compared to (0.353 ± 0.002) ps at angle larger than 10^0.....45

Figure 4.5: Relationship between the compressor setting and the maximum $\Delta T/T_0$ (a) and the FWHM (b) of the pump-probe cross correlation signal.....46

Figure 4.6: 800nm-800nm autocorrelation signal with FWHM of (109 ± 1) fs.....47

Figure 4.7: 400nm-800nm cross correlation signal with FWHM of (230 ± 9) fs.....48

Figure 4.8: The total temporal broadening obtained experimentally compared to the one calculated using GVD. Inset: Calculated temporal broadening for different optical elements.....50

Figure 4.9: The relative delay time obtained experimentally for different wavelengths compared to the expected one from GVD. Inset: Relative delay time expected from each optical components.....51

Figure 5.1: (a) Amorphous silicon films (b) Polycrystalline silicon films.....52

Figure 5.2: Transmission spectra of a-Si (a) and pc-Si (b) at different wavelengths.....54

Figure 5.3: Time resolved differential transmittance signals at different probe wavelengths for a-Si (a) and pc-Si (b) for film thickness of 100 nm and incident pump fluence of 0.54 mJ/cm^2.....56

Figure 5.4: Differential absorbance signal for different film thicknesses of pc-Si at pump fluence of 1.63 mJcm^2 and λ_{probe} = 630 nm.....58

Figure 5.5: The transmission spectra of 0.5 μm silicon on sapphire film before excitation (solid curve), at probe delay times of 0.5 ps and 200 ps. At 0.5 ps, there is a blue shift of fringes and a strong absorption caused by the presence of dense electron hole plasma. At 200 ps, there is a red shift caused by lattice heating (Downer and Shank 1986).....59

Figure 5.6: (a) Time resolved negative differential transmittance spectra at different probe wavelength for the 10 nm pc-Si film and incident pump fluence of 0.68 mJ/cm^2. (b) The carrier relaxation time as a function of the probe wavelength.....60

Figure 5.7: (a) Examples of negative differential transmittance spectra at different pump fluence. (b) Maximum absolute change of negative differential transmittance. (c) Measured photoinduced carrier relaxation time at different pump fluence as a function of carrier density.....63

Figure 5.8: Photoluminscense spectrum of silicon nanocrystal silicon film.....64

Figure 5.9: (a) Time resolved negative differential transmittance signal in the silicon nanocrystals film at different probe wavelengths and incident pump fluence of 0.40 mJ/cm^2 (b) The relaxation of the negative differential transmittance is fit to biexponential decay function. (c) The same decay is plotted on a log-linear scale.....66

Figure 5.10 (a) Time resolved negative differential transmittance signal at different pump fluences. (b) The negative differential transmittance amplitude at 0.3 ps and 16 ps probe delay times.....68

Figure A.1: Group index as a function of wavelength in 10 mm of water.....74

Figure A.2: Temporal broadening of pulses at different central wavelength in 10 mm of water.....74

Figure A.3: Relative time delay of different pulses of different central wavelength propagating in 10 mm of water.....74

Figure A.4 Transmission through the 600 nm narrow bandwidth filter. Inset: A Gaussian fit results in FWHM = (8.9 ± 0.2) nm.....75

Figure B.1: Two transient absorption signals for two scans of the same pump fluence and probe wavelength.....76

Figure B.2: Two different scans with different probe fluence.....77

Figure B.3: Illustration of the effect of residual signal at different pump fluences.....78

Figure B.4: Stimulated emission check for the 10 nm polycrystalline film and probe wavelength 630 nm.....79

List of Symbols

Name	Symbol
Absorption Coefficient	α
Amorphous Silicon	a-Si
Autocorrelation Function	ACF
Background Dielectric Constant	ε
Band Pass	BP
Beta barium borate	BBO
Complex Refractive Index	$\tilde{n}$
Cross Correlation Function	CCF
Decorrelation Factor	γ
Differential Transmittance	ΔT
Electric Field	$\vec{E}$
Energy Band Gap	E_g
Extinction Coefficient	κ
Frequency Bandwidth	$\Delta\omega$
Full-Width-at-Half-Maximum	FWHM
Group Index	N_g
Group Velocity Dispersion	GVD
Heat Capacity	ρC
Infrared	IR
Initial Carrier Density	N_0
Intensity	I
Length of Medium	L
Linear Frequency Bandwidth	$\Delta\nu$
Linear Refractive Index	n_0
Material Dispersion Coefficient	D_m
Nonlinear Refractive Index	n_2
Neutral Density	ND
Permittivity of Free Space	ε_0
Phase Velocity	v_p
Photoluminescence	PL
Polarization	$\vec{P}$
Polycrystalline Silicon	pc-Si
Probe Delay Time	τ
Propagation Constant	k
Pulse Bandwidth	$\Delta\lambda$
Pulse Duration	Δt

Pump Pulse Fluence	F
Pump Supercontinuum Probe	PSCP
Reduced Effective Mass	m^*
Refractive Index	n
Silicon Nanocrystals	Si-NCs
Speed of Light	c
Supercontinuum	SC
Supercontinuum Generation	SCG
Susceptibility	χ
Time Dependent Phase	$\phi(t)$
Wavelength	λ

1 Introduction

1.1 Motivation for Studying Ultrafast Carrier Dynamics in Silicon Nanostructures

Silicon is the most commonly used semiconductor in the microelectronics industry. Its electronic, mechanical and thermal properties, as well as the techniques for its processing are well understood. However, recent advances in information and communications technology resulted in the need of adding optical functionality to silicon-based electronic devices, since optical signal processing and transmission is thought to be a solution to overcoming limitations to the operating speed of microelectronic devices. Until recently, silicon has been considered unsuitable for use in optical devices due to its indirect bandgap, which results in its extremely low efficiency as a light emitter. The discovery of room-temperature light emission in nanostructured Si materials such as porous Si, Si nanocrystals (Si-NCs), and silicon-insulator superlattices prompted a great deal of research into the optical properties of Si nanostructures aimed at understanding the mechanisms of light emission and improving its efficiency. An additional benefit of nanostructured materials compared to bulk counterparts is the faster response time which holds promise of high speed Si-based optoelectronic devices (Othonos 1998). However, advancement in this field would require a clear understanding of the dynamics of charge carriers in these structures from their excitation from the equilibrium state to their subsequent relaxation. These dynamics occur on a wide range of time scale from femtoseconds to microseconds. In this thesis, we study the ultrafast carrier dynamics in polycrystalline and amorphous silicon thin films as well as silicon nanocrystal thin films using an optical pump – supercontinuum probe (PSCP) technique.

1.2 Ultrafast Carrier Dynamics in Semiconductors

In bulk semiconductors, conduction and valence bands are separated by an energy gap E_g (Fig. 1.1). At low temperatures and in the absence of external excitation, the conduction band is empty and the valence band is full. Absorption of a photon of energy exceeding E_g excites an electron to the conduction band, leaving a hole in the valence band. These photoexcited carriers then relax to equilibrium by means of thermalization and cooling to the lattice temperature. There are several processes that contribute to the energy and momentum relaxation, such as carrier-carrier scattering, intervalley and intravalley scattering, optical phonon scattering and carrier diffusion (Othonos 1998). The characteristic time of various relaxation processes ranges from several femtoseconds to a few picoseconds until the carriers reach the band edge of their respective band. At the band edge, the carriers are thermalized and have the same temperature as the lattice. At this stage, there is still an excess of electrons and holes compared to the thermodynamic equilibrium of the system. Therefore, electron-hole pairs can recombine and emit a photon in the process called radiative recombination. In direct band materials such as cadmium selenide and cadmium sulfide, electrons at the conduction-band minimum can recombine directly with holes at the valence band maximum, while conserving momentum. In indirect band gap semiconductors such as silicon, band edges occur at different points in the momentum space. In order to satisfy energy and momentum conservation, an electron and a hole can recombine and emit a photon only if this process is accompanied by emission of a phonon. This is the underlying reason behind low optical efficiency and long recombination times (microseconds) in bulk silicon compared to hundreds of picoseconds to several nanoseconds radiative lifetimes of charge carriers in direct band gap materials.

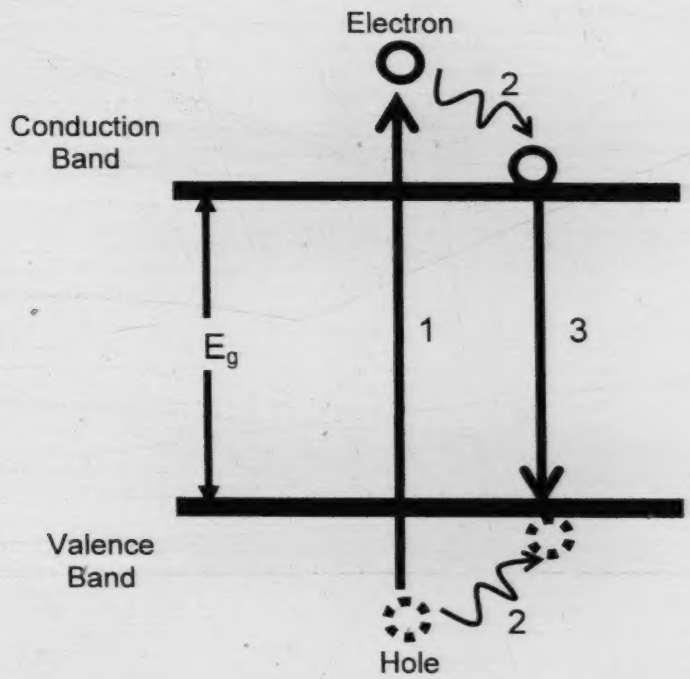

Figure 1.1: Photoexcitation and relaxation of carriers in bulk semiconductors. (1) Excitation of electrons to the conduction band. (2) Relaxation of electrons to the conduction band edge and holes to the valence band edge (3) Recombination of electrons in the conduction band with holes in the valence band.

In semiconductor nanocrystals, quantum confinement effects lead to the modification of the band structure by the formation of discrete energy states with energies determined by the size of the nanoparticles (Gaponenko 1998, Klimov 2003). Confinement of the electrons and holes within the small volume of the nanocrystal leads to increased overlap of electron and hole wavefunctions, and hence an enhanced radiative recombination probability. In addition, due to the large surface to volume ratio of the nanocrystals, energy states associated with the nanocrystal surface or interface play an important role in properties of these materials. Charge carriers in the nanocrystals can become trapped in the surface states, which typically exist within the bulk band gap. Trapping time constants for semiconductor nanoparticles range from hundreds of femtoseconds to

several picoseconds (Wu and Zhang 2004). From the trap states, carriers can recombine either radiatively (with emission of a photon) or nonradiatively (with emission of phonons).

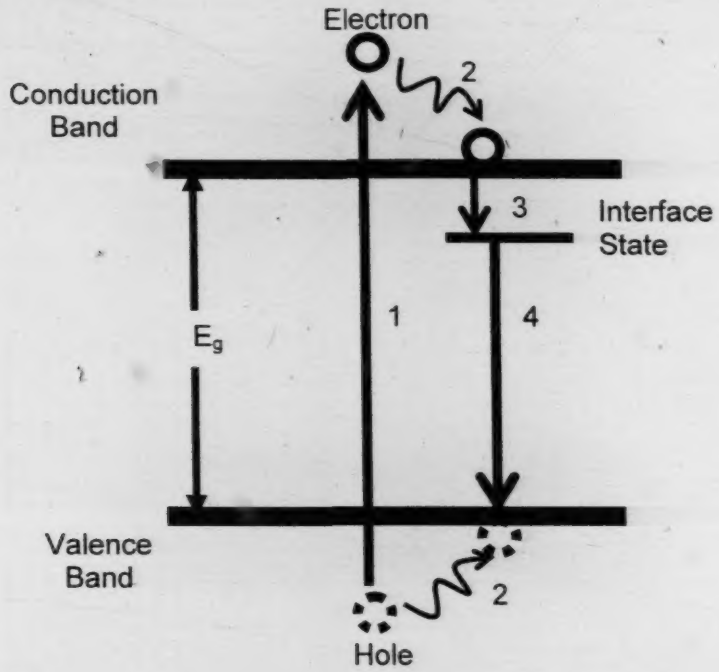

Figure 1.2. Photoexcitation and relaxation of semiconductor nanocrystals. (1) Excitation of electrons to the conduction band. (2) Relaxation of electrons to the conduction band edge and holes to the valence band edge. (3) Trapping of carriers in the interface states (4) Recombination of electrons in the interface states with holes in the valence band. (Adapted from Pavesi *et al.*, 2000).

At carrier densities larger than 10^{20} cm^{-3}, the non-radiative three-particle Auger recombination process becomes important (Othonos 1998). In this process, an excited electron recombines with a hole and gives its energy to another electron, which is hence excited to higher energy states (Fig. 1.3).

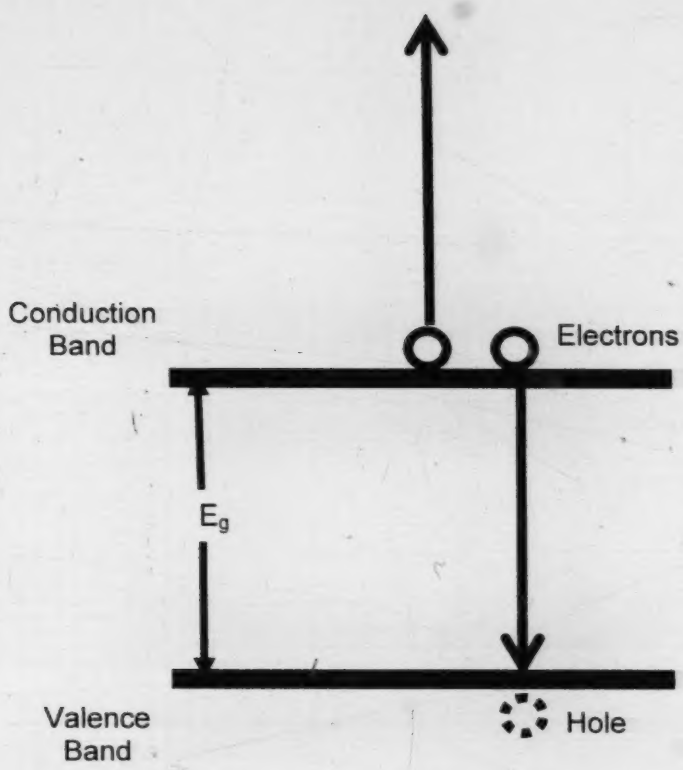

Figure 1.3: Auger process. (Adapted from Pavesi, 2006).

1.3 Pump-Probe Technique

One of the most common techniques used to study ultrafast processes in semiconductors is the optical pump – optical probe technique (see Fig. 1.4). This method allows probing the carrier dynamics with a time resolution limited only by the laser pulse width. The laser pulse is split into two, a larger intensity pulse used to excite the sample and a weaker pulse which probes the changes induced in the sample by the pump pulse. The probe pulse has to be weak enough to provide minimum perturbation to the sample. Transmission or reflection of the probe pulse from the sample is detected as a function of time. The time evolution of the probe signal is obtained by varying an optical delay time using a computer controlled translation stage as shown in Fig. 1.5. The detailed description and characterization of the experimental setup used for the ultrafast pump-

probe measurements of the carrier dynamics in silicon thin films studied in this thesis will be given in Chapters 2 and 3.

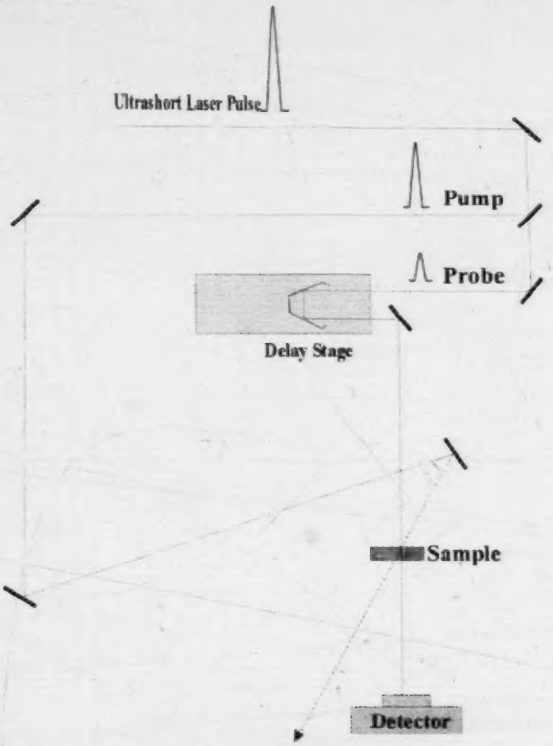

Figure 1.4: Schematic diagram of the pump-probe technique.

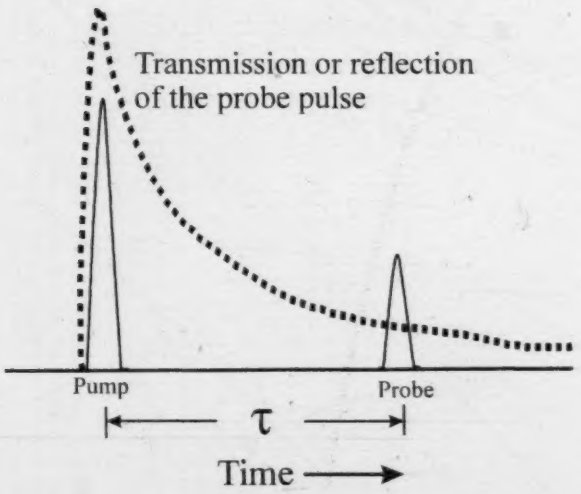

Figure 1.5: Time evolution of the transient transmission or reflection signal in a pump probe experiment. (Modified from Andor technology catalogue).

Using pump and probe beams of the same wavelength, the dynamics of carrier scattering out of their excited energy distribution can be monitored. On the other hand, using variable wavelength probe allows extension of carrier dynamics studies to the relaxation of the carrier distribution (Lin et al. 1988).

In equilibrium, the complex refractive index of the sample can be described by

$$\tilde{n} = n + i\kappa, \qquad (1.1)$$

where n is the refractive index, κ is the extinction coefficient and $i = \sqrt{-1}$.

Excitation of the sample with photons of above band gap energy creates a non-equilibrium distribution of carriers. The initial photoexcited carrier density, N_0, can be calculated by

$$N_0 = (1 - T_{pump} - R_{pump})\frac{\alpha F}{h\nu}, \qquad (1.2)$$

where T_{pump} is the transmissivity of the pump pulse, R_{pump} is the reflectivity of the pump pulse, F is the pump pulse fluence, α is the optical absorption coefficient of the pump pulse and $h\nu$ is the photon energy at the specific pump wavelength.

At low excitation levels ($N_0 < 10^{20}$ cm^{-3}), the increase of the sample temperature by direct heating of lattice by emission of phonons is given by (Tanaka et al. 1997)

$$\Delta T_e = \frac{(1 - T_{pump} - R_{pump})\alpha F}{\rho C} \cdot \frac{(h\nu - E_g)}{h\nu}, \qquad (1.3)$$

where ρC is the heat capacity of the sample in $Jcm^{-3}K^{-1}$.

At high excitation levels ($N_0 > 10^{20} cm^{-3}$), lattice heating increases due to Auger recombination (Downer and Shank 1986).

Due to the change in free carrier density and temperature of the sample, the refractive index is modified. The total change in refractive index, Δn, is equal to (Othonos and Christofides 2002)

$$\Delta n = \Delta n_N + \Delta n_{\Delta T_e} = \frac{\partial n}{\partial N}\Delta N + \frac{\partial n}{\partial T_e}\Delta T_e , \qquad (1.4)$$

where Δn_N and $\Delta n_{\Delta T_e}$ are the carrier density and temperature contributions to Δn, respectively.

The carrier density contribution to Δn, can be estimated from Drude expression (Doanay and Grischkowsky 1987)

$$\Delta n_N = -(\frac{2\pi e^2}{\varepsilon m^* \omega^2})Nn_0, \qquad (1.5)$$

where ε is the background dielectric constant, m^* is the reduced effective mass for electrons and holes, ω is the probe angular frequency, and N is the carrier density.

Similarly, the total change in extinction coefficient, $\Delta\kappa$, is equal to

$$\Delta\kappa = \Delta\kappa_N + \Delta\kappa_{\Delta T_e} = \frac{\delta\kappa}{\delta N}\Delta N + \frac{\delta\kappa}{\delta T_e}\Delta T_e, \qquad (1.6)$$

where $\Delta\kappa_N$ and $\Delta\kappa_{\Delta T_e}$ are the carrier density and temperature contributions to $\Delta\kappa$, respectively.

Relaxation of these free carriers back to equilibrium and the temperature evolution can be monitored by the probe pulse. The reflection and transmission of the probe pulse are affected by the changes in refractive index and extinction coefficient. If the experiment is

performed in the transmission mode, the monitored quantity is the differential transmission (Maly 2002)

$$\frac{T-T_0}{T_0}=\frac{\Delta T}{T_0}, \qquad (1.7)$$

where T is the transmission of the probe in the presence of the pump pulse, while T_0 is the transmission in the absence of the pump pulse. The measured differential transmission, ΔT, is due to change in reflectivity and absorption.

As an approximation, we considered that ΔT is solely due to the absorption of the probe in the sample. In this case, the absorption can be related to differential transmission according to

$$T=T_0e^{-A}=T_0e^{-\alpha l}, \quad (1.8)$$

where α is the absorption coefficient of the sample ($\alpha=\frac{4\pi\kappa}{\lambda}$), and l is the length of the sample. Further treatment yields the following

$$\frac{T-T_0}{T_0}+1=e^{-\alpha l}$$

$$-\ln(\frac{\Delta T}{T_0}+1)=\alpha l. \qquad (1.9)$$

Using the series expansion $\ln(x+1)=x-\frac{x^2}{2}+\frac{x^3}{3}-\frac{x^4}{4}+...$, where $x=\frac{\Delta T}{T_0}$ and for $\frac{\Delta T}{T_0}<<1$, the above expression can be approximated as

$$-\frac{\Delta T}{T_0}\approx\alpha l. \qquad (1.10)$$

In this thesis, we will consider that the change in transmission of the probe pulse is solely due to change in absorption unless otherwise specified.

Depending on the wavelength of the probe pulse, the dynamics of different carrier energy states can be investigated. For the wavelengths close to the pump wavelength, a decrease in absorption is observed as a result of bleaching of the interband transitions by the pump pulse. After this decrease, the absorption signal decays to its unperturbed value due to scattering of the carriers out of their initial photoexcited states by carrier-carrier or carrier-phonon scattering, as illustrated in Fig. 1.6. This initial bleaching of states has been observed in some semiconductors like GaAs (Lin et al. 1988, Behren et al. 1996).

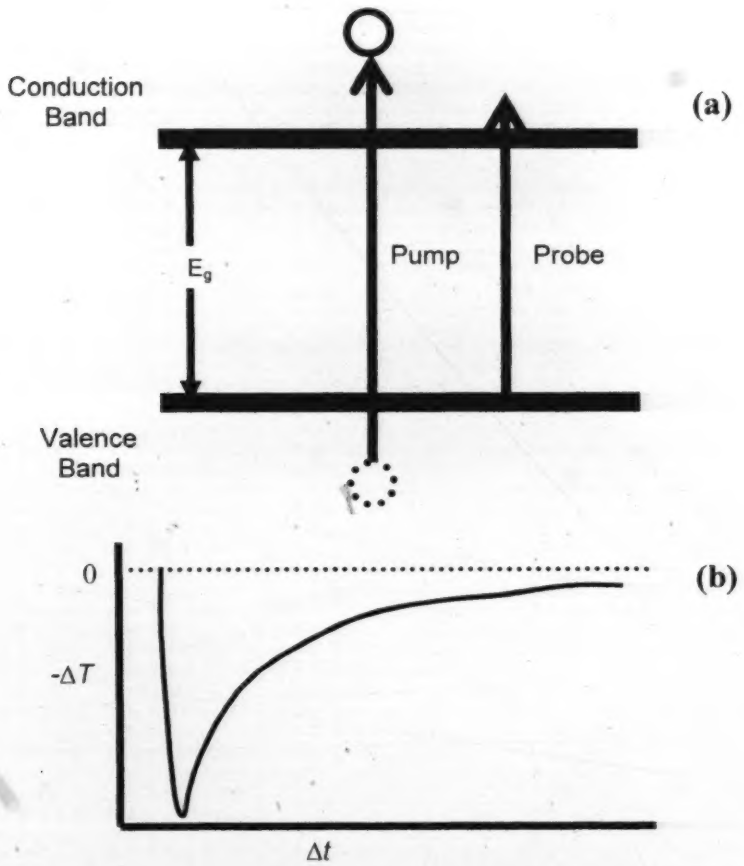

Figure 1.6: (a) Bleaching of interband transitions by pump pulse. (b) The corresponding transient absorption signal with initial decrease in absorption of the probe beam.

On the other hand, the increase in absorption observed at different probe energies is the result of free carrier absorption and absorption by carriers trapped in the midgap states such as interface states (Fig. 1.7) (Forst et al. 2007).

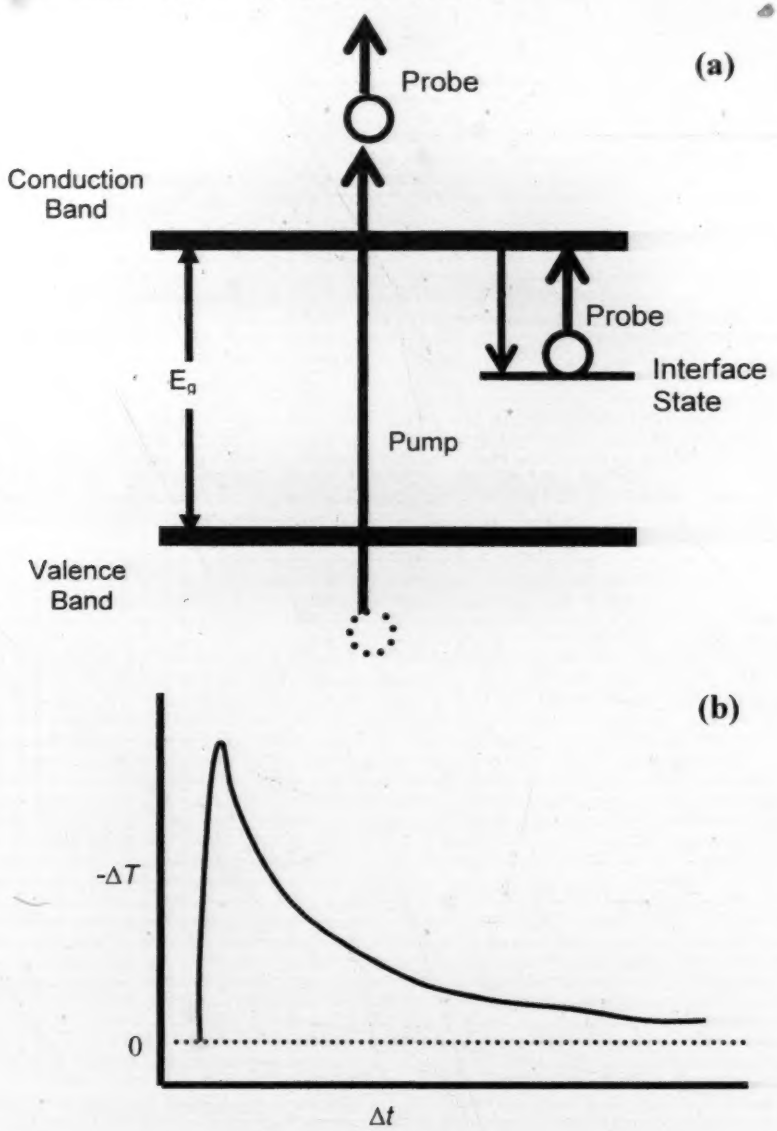

Figure 1.7: (a) Absorption of the probe pulse by the free photoexcited carriers and by carriers trapped in the interface states. (b) The corresponding transient absorption signal with initial increase in the absorption of probe beam.

1.4 Previous Work

The ultrafast carrier dynamics in semiconductors has been a subject of extensive research in the past two decades (Lioudakis et al. 2006). Detailed knowledge of the various dynamical processes such as photoexcitation of carriers in semiconductors, carrier thermalization, and energy and momentum relaxation of the photoexcited carriers is the prerequisite for the development of new high-speed optoelectronic devices. Recently, these studies have been extended to the ultrafast carrier dynamics in silicon. While silicon is the material of choice for microelectronics, and its electronic, thermal and mechanical properties are well known, the understanding of its ultrafast optical properties is incomplete. With silicon being an indirect band gap material, studies of its optical properties and the interpretation of the experimental results are challenging (Lee et al. 1998).

The discovery of the room temperature optical emission from porous silicon by Canham et al in 1990 which was attributed to the quantum confinement of carriers in the nanoscale silicon structures within porous Si (Canham 1990), motivated a lot of research in synthesis of various types of light-emitting silicon nanostructures. One of the most widely researched structures is silicon nanocrystals embedded in a silicon dioxide matrix. In this structure, silicon nanocrystals are protected from contamination and oxidization by air due to the stability of the Si/SiO_2 interface, which leads to stable PL emission (Tripathy et al. 1998, Lockwood and Pavesi 2004). The first photoluminescence obtained from this structure was reported by Osaka *et al.* in 1992. However, the origin of the photoluminescence in this system is still under debate. It is believed that the light emission in silicon nanocrystals cannot be attributed to the quantum confinement of charge carriers, as the theoretically predicted emission properties in this case significantly differ from the experimental results (Huy et al. 2006). The Si/SiO_2 interface states were proposed as a mechanism for explaining photoluminescence in silicon nanocrystals (Pavesi et al. 2000). Both experimental (Klimov et al. 1998) and theoretical approaches (Hadjisavvas and Kelires 2004, Luppi and Ossicini 2005) arised to study this mechanism.

The study of carrier dynamics just after excitation and before the PL emission is essential to clarify the light emission mechanism in this system. Previous studies have found evidence of the two different mechanisms of photoexcited carrier relaxation (Klimov et al. 1998 a, Liodakis et al. 2007). The fast mechanism was attributed to carriers trapped at interface states at the nanocrystal boundary, while the slow mechanism was attributed to the quantized states in the interior of the nanocrystals. In our lab, carrier dynamics in silicon nanocrystals were studied using optical pump terahertz probe technique (Cooke et al. 2006). This study confirmed the previous findings that the Si/SiO_2 interface plays an important rule in trapping of photoexcited carriers. In this thesis, we will continue investigations of the ultrafast carrier dynamics in silicon nanocrystals using a new experimental setup: an optical pump - supercontinuum probe experiment. In chapter 2, we will provide a brief overview of the ultrafast optics necessary for understanding the experimental techniques used in this study. In chapter 3, the experimental setup will be described in detail. In chapter 4, we will characterize this setup before proceeding further to the discussion of the experimental results of studies of carrier dynamics in nanostructured silicon films in chapter 5. In chapter 6, the conclusions will be drawn, and the future research directions will be outlined.

2 Propagation and Measurement of Ultrashort Pulses

Before we discuss the details of the experimental setup used for the PSCP measurement and its subsequent characterization, we first need to give a brief introduction to ultrashort optical pulses.

2.1 Ultrashort Laser Pulses

An ultrashort light pulse is a pulse with time duration less than 1 ps. Only a small number of optical cycles fit under the intensity envelope of such a pulse. Ultrashort pulses are widely used in spectroscopy due to their high peak intensities and short duration. They can be generated by mode-locked lasers. To obtain pulses short in time, a broad spectral bandwidth is required according to the following

$$\Delta t \Delta \omega \geq \frac{1}{2}, \qquad (2.1)$$

where Δt is the pulse duration and $\Delta \omega$ is the frequency bandwidth of the pulse. When the equality is reached in this relation, the short pulse is said to be bandwidth limited. Experimentally, it is easier to measure the full width at half maximum (FWHM) values of pulse duration and frequency. The time bandwidth limited value is different for different pulse shapes. For a Gaussian pulse, this product becomes

$$\Delta t \Delta \nu \sim 0.441, \qquad (2.2)$$

where

$$\Delta \nu = \frac{c}{\lambda^2} \Delta \lambda, \qquad (2.3)$$

Here $\Delta\nu$ is the linear frequency bandwidth of the pulse, c is the speed of light, λ is the central wavelength of the pulse, and $\Delta\lambda$ is the pulse bandwidth. Bandwidth limited pulses have the shortest pulse duration possible for their spectral bandwidth.

2.2 Propagation of Short Pulses in the Linear Optics Regime

In linear optics, the induced polarization in a medium is linear with the electric field of the light as it traverses that medium. The relation that describes this fact is

$$\vec{P} = \varepsilon_0 \chi \vec{E}, \qquad (2.4)$$

where $\vec{P}$ is the induced polarization in the sample, χ is the susceptibility of the medium, ε_0 is the permittivity of free space and $\vec{E}$ is the electric field of the pulse. In this regime, we will focus on the effect of group velocity dispersion (GVD) on the propagation of ultrashort pulses. In the linear regime, GVD is manifested by the broadening of the pulse envelope when a pulse is propagated through a transparent medium. Although GVD results in nonlinear optical effects as well, they will not be discussed in this thesis. Interested readers can refer to Walmsley *et al.*, 2001.

Two different velocities can describe the propagation of ultrashort pulses. The phase velocity v_p describes the speed of the frequency components of the pulse and can be calculated from

$$v_p = \frac{\omega}{k}, \qquad (2.5)$$

where k *is* the propagation constant and ω is the angular frequency.

The group velocity, v_g, is the velocity of the pulse envelope and is equal to

$$v_g = \frac{d\omega}{dk}, \qquad (2.6)$$

or, in terms of the group index N_g,

$$v_g(\lambda) = \frac{c}{N_g}, \tag{2.7}$$

$$v_g(\lambda) = \frac{c}{n(\lambda) - \lambda \frac{dn(\lambda)}{d\lambda}}, \tag{2.8}$$

where n is the refractive index of the medium.

GVD is the wavelength dependence of the group velocity, and it is characterized by the material dispersion coefficient

$$D_m \approx \frac{-\lambda}{c}\frac{d^2n}{d\lambda^2} \approx -\frac{1}{c}\frac{dN_g}{d\lambda}. \tag{2.9}$$

If D_m is negative, the material is said to have positive GVD, and vise versa. If the GVD is positive, higher frequency (shorter wavelength) components of the pulse travel slower than the lower frequency (larger wavelength) components. Conversely, in materials with the negative GVD, the lower frequency components of the pulse propagate slower. Whether GVD of the various optical elements is positive or negative, it results in the temporal broadening of the pulse as it goes through them. This broadening can be calculated as

$$\Delta t = |D_m| L \Delta\lambda, \tag{2.10}$$

where L is the length of the medium .The calculated broadening is therefore due to material dispersion (Kasap 2001).

The difference in propagation time for different component wavelengths in the pulse can also be calculated from GVD as the following

$$\Delta t_d = \frac{L}{v_g(\lambda_i)} - \frac{L}{v_g(\lambda_0)}, \qquad (2.11)$$

where λ_0 is the arbitrarily chosen reference wavelength and λ_i is the wavelength of interest(Dong-Hui et al 2003).

2.3 Propagation of Short Laser Pulses in the Nonlinear Regime

At very high light intensities, the induced polarization in a material is no longer a linear function of the electric field of light and can be expanded in a power series

$$\vec{P} = \varepsilon_0(\chi_1 \vec{E} + \chi_2 \vec{E}\vec{E} + \chi_3 \vec{E}\vec{E}\vec{E} + \ldots). \qquad (2.12)$$

Here, the coefficients χ_n represents the nth-order susceptibilities of the medium. The terms involving high-order terms of electrical field give rise to the nonlinear processes. The second-order susceptibility is non-zero only in materials with no inversion symmetry, whereas the third-order nonlinearity can be observed in all materials, including those with inversion symmetry.

One of widely used applications of the second-order nonlinearity is second harmonic generation. For example, a 400 nm beam can be obtained by focusing an 800 nm beam into a second-order nonlinear crystal such as beta-barium borate (BBO) (Rulliere 1998).

Third-order nonlinearity results in many interesting phenomena such as four-wave mixing, Raman scattering and the optical Kerr effect. Here we will concentrate on the optical Kerr effect since it has particular importance to the experiments described in this thesis.

In the optical Kerr Effect, the third-order nonlinearity results in an intensity-dependent refractive index that can be described by the following equation

$$n(t,x) = n_0 + n_2 I(t,x). \qquad (2.13)$$

Here, n_0 is the linear refractive index, n_2 is the nonlinear refractive index and I is the pulse intensity.

One of the important consequences of optical Kerr effect is self-phase modulation. When an intense ultrashort pulse propagates in a medium, the time varying induced refractive index results in a time dependent phase modulation, $\phi(t)$, given by

$$\phi(t) = \omega_0 t - \frac{2\pi n}{\lambda} l = \omega_0 t - \frac{2\pi l}{\lambda}\left[n_0 + n_2 I\right], \qquad (2.14)$$

where l is the distance traveled in the medium. Because of the phase modulation, different frequency components of the pulse will experience different phase shift resulting in the generation of new frequencies. This can be described by the following equation (Eaton 1993)

$$\omega = \frac{d\phi}{dt} = \omega_0 - \frac{2\pi n_2 l}{\lambda}\frac{dI(t)}{dt}. \qquad (2.15)$$

For a Gaussian pulse, the leading edge of the pulse will be shifted to lower frequencies while the trailing edge will be shifted to higher frequencies as shown in Fig 2.1. As a result, the pulse will broaden in its frequency spectrum. It is clear that for a symmetric pulse, the spectrum broadening will be symmetric as well.

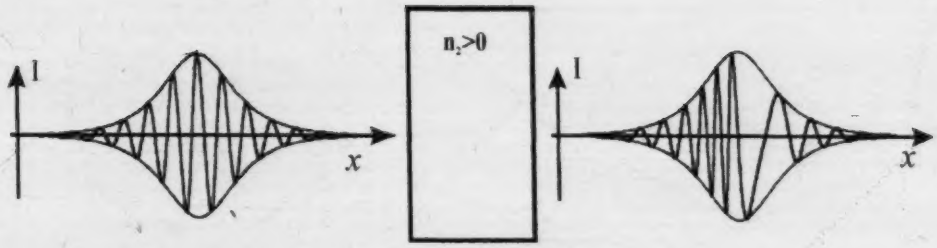

Figure 2.1: Self phase modulation (Modified from Steinmeyer *et al.*, 1999).

Optical Kerr effect can also result in self-focusing of the beam. This effect is illustrated in Figure 2.2. An ultrashort pulse has a higher intensity in its center than the edges. Therefore, when a propagating pulse experiences a nonlinear refractive index, it results in focusing the pulse toward its centre. For self-focusing to occur, laser power of a Gaussian beam has to exceed a critical power of (Marburger 1975)

$$P_{cr} = \frac{3.77\lambda^2}{8\pi n_0 n_2} \qquad (2.16)$$

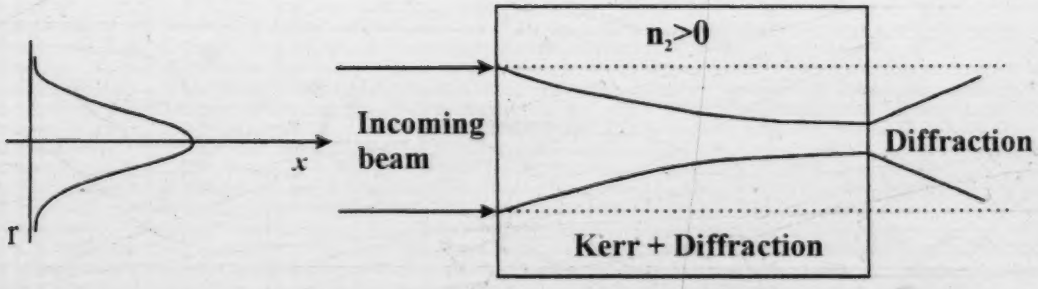

Figure 2.2: Self-focusing of ultrashort pulse (Adapted from Antoncini).

2.4 Supercontinuum Generation

Propagation of intense laser pulses in non-linear media leads to the interesting phenomenon of supercontinuum generation (SCG), i.e. conversion of laser light to light with broad spectral bandwidth. SCG is achieved by focusing intense laser pulses into a transparent medium, which can be a solid (Midorikawa et al. 2001), liquid (Dharmadhikari et al. 2004) or gas (Akozbek et al. 2001). The spectrum of the resulting supercontinuum (SC) can extend from the ultraviolet to the infrared region, depending on several parameters. Some of these parameters are related to the medium characteristics such as the band gap (Brodeur and Chin 2001) and length, while others depend on the generating pulse properties such as wavelength (Nagura et al. 2002), power, temporal duration and polarization state (Dharmadhikari et al. 2004). Although the procedure to obtain white light is very simple and straightforward, the exact physics behind it is not well understood. Since the first supercontinuum was generated by Alfano and Shapiro (Alfano and Shapiro 1970), there has been a substantial effort in trying to understand the key mechanisms behind this process. The broad frequency distribution of the SC indicates that self phase modulation may be its generation mechanism. However, SPM predicts that the spectrum produced is symmetric but the asymmetry exists in most white light spectra, with the blue side of the spectrum extended more than the red in most cases. This suggests that there are other mechanisms responsible for SCG. SCG is only produced at powers exceeding the critical power of self-focusing, and therefore self-focusing was proposed as a generating process. Self-steeping, group velocity dispersion and multiphoton excitation (Brodeur and Chin 1997) are some of the other suggested mechanisms. It is widely accepted now that more than one nonlinear mechanism is responsible for SCG. Due to its unique coherent, continuous broadband spectrum, SCG has found uses in many applications including optical parametric amplification, optical pulse compression, and PSCP spectroscopy.

PSCP spectroscopy has been used extensively for studying carrier dynamics in different materials due to a wide range of probe wavelength tunability. However, the use of SC as a probe is not straight-forward (Klimov and McBranch 1998b). SC is considerably

chirped due to GVD in the medium in which it is generated as well as in other optical elements (see eq. 2.11) (Yamaguchi and Hamaguchi 1995). This results in the broadening of the laser pulse from few femtoseconds to several picoseconds hindering its use in femtosecond spectroscopy. In the following sections, we will explain some approaches to overcoming this difficulty.

2.5 Measurements of Ultrashort Pulses

It is important to characterize ultrashort pulses before using them for experiments. Pulse duration, shape, intensity, spectral composition and chirp have to be well determined.

The general rule is that in order to measure an event in time, you have to use an equal or a shorter event. Due to the extremely short duration of these pulses, it is difficult to measure them using relatively slow electronic measuring devices. Therefore, it is necessary to resort to techniques that use the ultrashort pulse to measure itself. In such techniques, the laser pulse is divided into two beams and then recombined again in a medium and allowed to interact via a nonlinear process. These can be second-order processes such as second harmonic generation (Chavez et al. 2005) or third-order processes like third harmonic generation (Eckardt and Lee 1969) and the optical Kerr effect (Dahlstorm and Kallberg 1971, Albrecht et al. 1992, Michelmann et al. 1996). In all of these methods, pulse characterization is performed using an intensity correlation function. Assumptions regarding the pulse shape have to be made prior to analysis (Ho and Alfano 1978).

When a second-order nonlinear crystal such as BBO is used as the interaction medium, the second harmonic pulse is generated from the combination of the two beams. If one pulse is delayed with respect to the other by a specific amount of time τ, the signal detected can be described by the following second-order correlation function (Peatross and Rundquist 1997)

$$G^{(2)}(\tau,0) = \int_{-\infty}^{\infty} I_{pump}(t) I_{probe}(t-\tau) dt \qquad (2.17)$$

There are some major drawbacks to the second-order correlation. This method does not provide information about the pulse intensity and the shape symmetry (Weber and Dandliker 1968). The use of the second order correlation is also limited due to the absence of appropriate second harmonic generation crystals in the ultraviolet region of the spectrum (Chavez 2005).

Most of these drawbacks can be avoided by using a third-order interaction such as the optical Kerr effect. The experimental setup for the optical Kerr gate measurements is illustrated in Fig. 2.3.

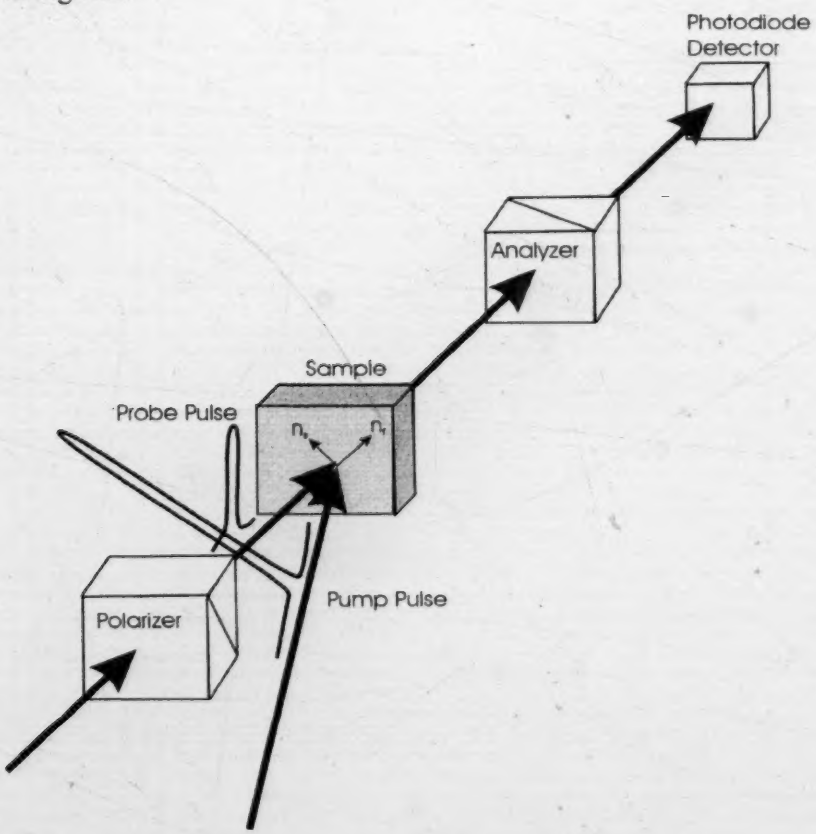

Figure 2.3: Optical Kerr Gate. (Adapted from Slepkov, 2002).

In this method, the sample is placed between two crossed polarizers. In the absence of the pump pulse, there is no transmission of the probe. An intense pump pulse with polarization set to 45 degrees relative to that of the probe pulse induces a birefringence in the medium. The change in the refractive index n is given by Eq. 2.13. This results in a change the polarization state of the probe from linear to elliptical (Alfano 1986), allowing some of the intensity to be transmitted through the analyzer. For best results, the response of the Kerr medium should be faster than the gating pulse width so that the gate resolution is solely determined by the gating pulse duration. Moreover, the gating pulse should be narrower than the probe pulse in order to be able to resolve the probe pulse duration. Optical Kerr gate gives rise to the third order correlation function (Takeda et al. 2000)

$$G^{(3)}(\tau,0) = \int_{-\infty}^{+\infty} dt I_{probe}(t-\tau) I_{pump}^{2}(t) \qquad (2.18)$$

If the pump and probe beams profiles are identical then this function represents the autocorrelation function (ACF) while if the two beams are different this function represents the cross correlation function (CCF). The probe pulse duration can be obtained from the decorrelation factor γ (Albrecht et al. 1992)

$$\gamma = \frac{\tau_{FWHM}}{\tau_{probe}} \qquad (2.19)$$

Here, τ_{FWHM} is the full width at half maximum of the intensity of the correlation function and τ_{probe} is the probe pulse duration. Fig.2.4 gives the value of γ as a function of the pump pulse duration τ_{pump} normalized to the correlation width τ_{FWHM}. For the autocorrelation, values of γ are located in the top end of the plot and equal to 1.22 and 1.29 for the Gaussian and $sech^2$ pulses respectively (Albrecht et al. 1992).

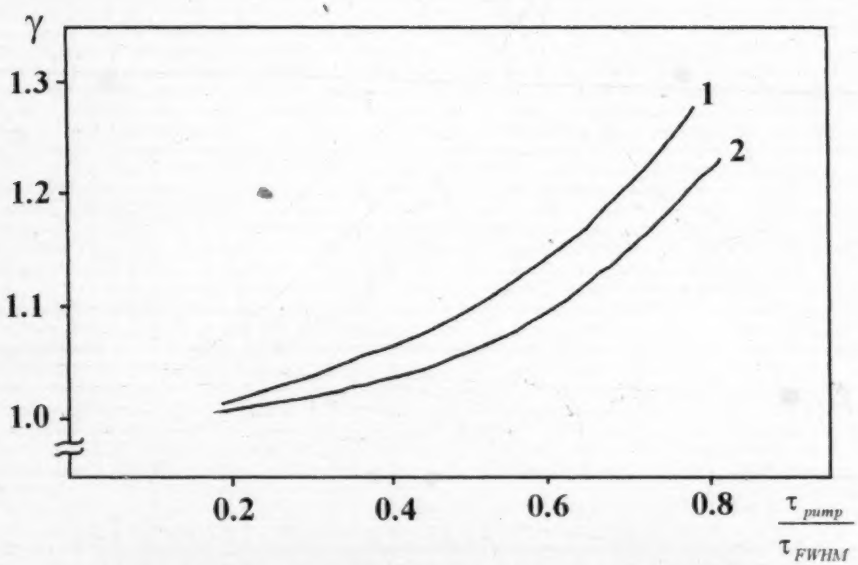

Figure 2.4: The decorrelation factor γ for sech^2 (1) and Gaussian (2) as a function of the normalized pump pulse duration to the FWHM duration of the correlation function (Adapted from Albrecht et al. 1992).

Unlike the second-order correlation, third-order correlation function reveals information about pulse asymmetry (Michelmann et al. 1996). It is applicable for pulse measurements in the broad spectral range from UV to near infrared in the UV. In this thesis, we use the optical Kerr gate and the third order correlation function for the ultrashort pulse characterization.

3 The PSCP Setup and Methodology

3.1 Experimental Layout

We utilized the pump and probe technique in our experiment. A detailed diagram of the experimental setup is shown in Fig 3.1. The source of the ultrashort pulses is an amplified Ti: sapphire laser system. The laser beam, which consists of a train of 100 fs pulses, each pulse centered at 800 nm and delivered at a repetition rate of 1.08 kHz, is split by a beam splitter into a high power beam used to excite the sample and a weaker beam used to probe the changes in the excited sample. To give a dynamic picture, the probe is delayed with respect to the pump by a delay stage, which is controlled by a labview computer program. The pump beam is focused into a BBO crystal for second harmonic generation and the resulting 400 nm pulses are focused onto the sample. The pump beam power and hence the initial carrier density in the sample is controlled by a half wave plate and polarizer combination. Any pump beam passing through the sample is blocked by an iris. The probe beam is focused into a 1 cm cell of flowing water for the SCG. The SC is then filtered to narrow bandwidth probe pulses using 10 nm bandwidth interference band pass filters. In this experiment, we used a set of filters with central wavelengths ranging from 450 nm to 700 nm. The probe beam is then further split into two beams using a 55% transmission / 45 % reflection pellicle beam splitter. One beam goes through the sample where it overlaps with the pump beam. The other beam does not go through the sample and acts as a reference for differential detection as will be discussed later. The signal of the two beams is detected by separate Si detectors that are connected to two lock-in amplifiers for phase sensitive detection. The pump beam is chopped mechanically at 540 Hz to turn the excitation of the sample on and off. A third lock-in amplifier detects the difference of the two detector signals. Signals from the three lock-in amplifiers are sent to a computer that is used for data acquisition and delay stage control. Pump and probe beams polarizations are perpendicular to each other to minimize interferences between the two beams at the sample (Doany et al. 1986).

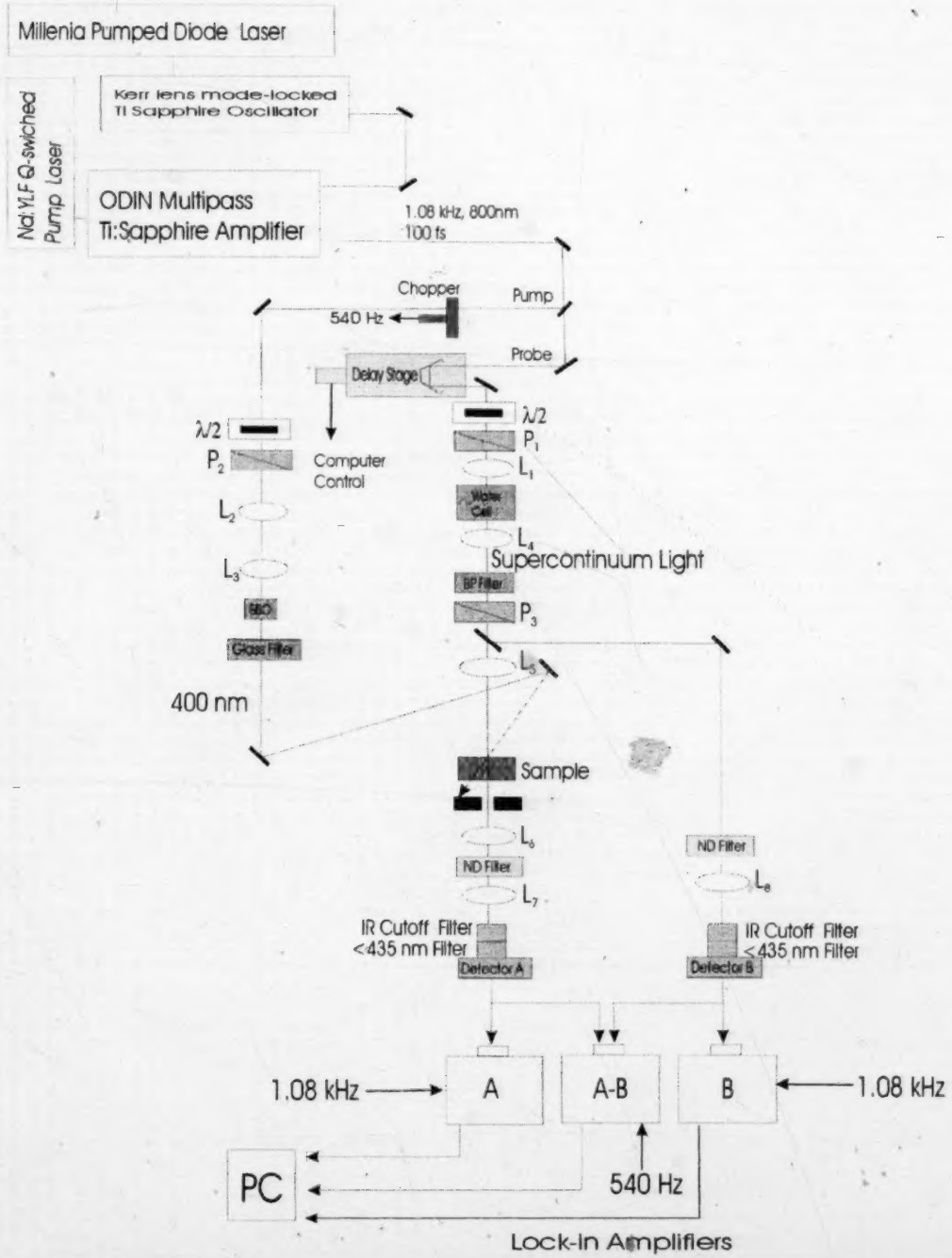

Figure 3.1: The PSCP setup. All optics are optimized for the corresponding wavelengths. λ/2: half wave plate, P_1,P_2:Polarizers, P_3: broadband Glan-laser polarizer, L_1=20cm lens, L_2=30cm lens, L_3=-10cm lens, L_4=7.5cm achromat doublet lens, L_5,L_6,L_7,L_8=10cm achromat doublet lenses. BP: Band Pass. IR: Infrared. ND: Neutral Density. PC: Personal Computer.

When applynig Kerr gate, we used two different configurations: One for determination of zero time delay, t_0 (when pump and probe pulses arrive the sample at the same time) and the other for pulse characterization.

To construct a Kerr gate for t_0 determination, a slight modification is applied to the setup as shown in Fig. 3.2. The probe beam polarization is set to 45° to the pump polarization and a polarizer set to 90 ° with respect to the polarization of the probe beam is added after the sample (see also Fig. 2.3). A 1 mm thick quartz slide, which is known to have an approximately instantaneous Kerr response, is used as a Kerr medium. All optics before the sample are kept the same as when performing PSCP experiments to provide an accurate determination of t_0.

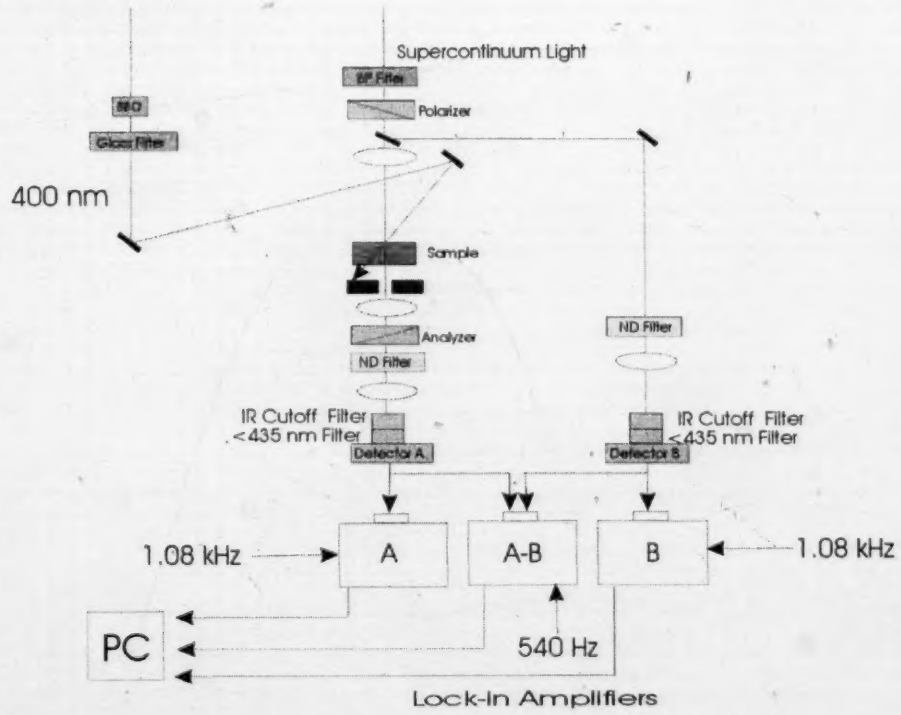

Figure 3.2: Optical Kerr Gate Setup for zero time delay measurement.

To construct a Kerr gate for pulse characterization, we removed the band pass filter before the sample and achieved the wavelength selection after the sample with two paired filters as shown in Fig 3.3. This was to ensure that all wavelength components of white light pass the same optical path before the sample.

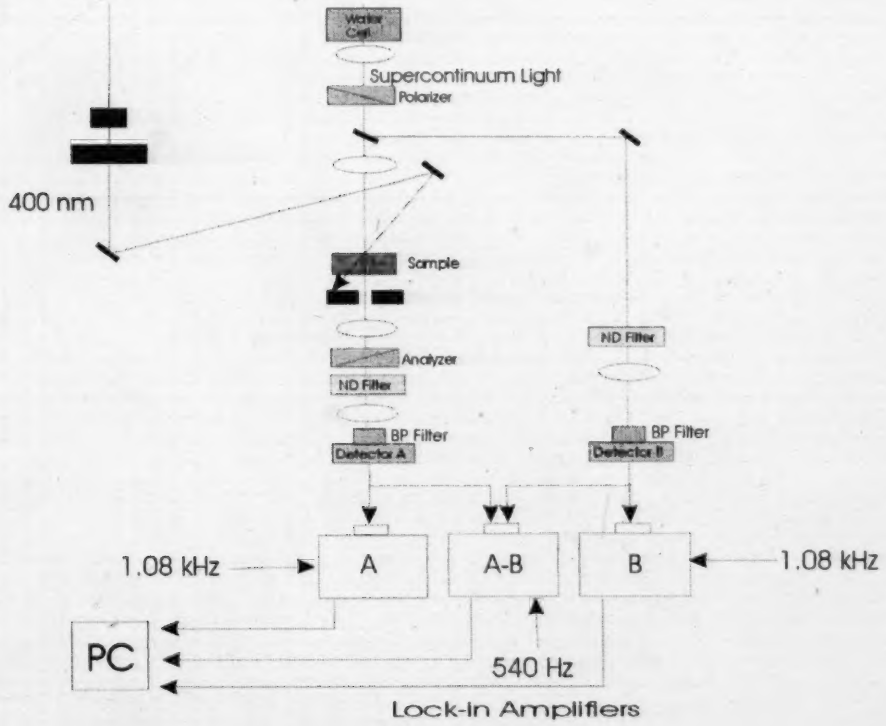

Figure 3.3: Optical Kerr Gate Setup for pulse characterization.

3.2 Data Acquisition and Experimental Considerations

3.2.1 Pump and Probe Beams Spatial Profile

It is important to overlap the probe and pump beams both spatially and temporally. The spatial overlap is achieved by focusing the probe beam into a spot that is smaller in size than that of the pump beam. This ensures that the probe is covered completely by the pump and a uniform excited area in the sample is being probed and studied. To study the spatial profiles of the pump and probe beams, a 10 μm pinhole was placed at the sample position and mounted on a two dimensional translational stage. Intensities of the beams transmitted through the pinhole were monitored by a photodiode that was connected to an oscilloscope. The resulting intensities as a function of the position of the pinhole relative to the optical axis are shown in Fig. 3.4. It is clear from this figure that the spatial profiles of both beams fit well to a Gaussian curve. Taking the diameter of the Gaussian to be equal to $1/e^2$ of its maximum, the diameters of the pump and the probe beams were found to be 0.933 mm and 0.578 mm, respectively. In this measurement, the entire spectral bandwidth of the white light continuum was used. For the actual transient absorption measurements, the white light was spectrally filtered as discussed earlier. However, spectral filtering does not have a significant impact on the size of the probe beam since the lenses used to focus it are achromatic. Simple calculations were performed to estimate fluences of both beams used in this experiment using the following equation

$$F = \frac{P_{ave}}{\pi \omega_0^2 f} \qquad (3.1)$$

where P_{ave} is the average laser power, f is the repetition rate of the laser, and ω_0 is the Gaussian radius of the beam at the sample position.

For the pump beam, the average power used in the experiments ranged from 1 mW to 13 mW, which corresponds to fluences ranging from 0.13 mJ/cm^2 to 1.7 mJ/cm^2. For the probe beam, we used filters to provide 10 nm bandwidth of wavelength instead of the whole white light. Since we are using achromatic doublets lenses to focus the white light, the diameter of these filtered probes is not expected to vary widely from the diameter of

the whole white light. The maximum fluence of these is near 700 nm wavelength and was approximately 17 $\mu J/cm^2$, while the minimum fluence was for the 450 nm and was approximately 2 $\mu J/cm^2$. We can see that the fluences of the pump beam are a lot higher than that of the probe as should be the case.

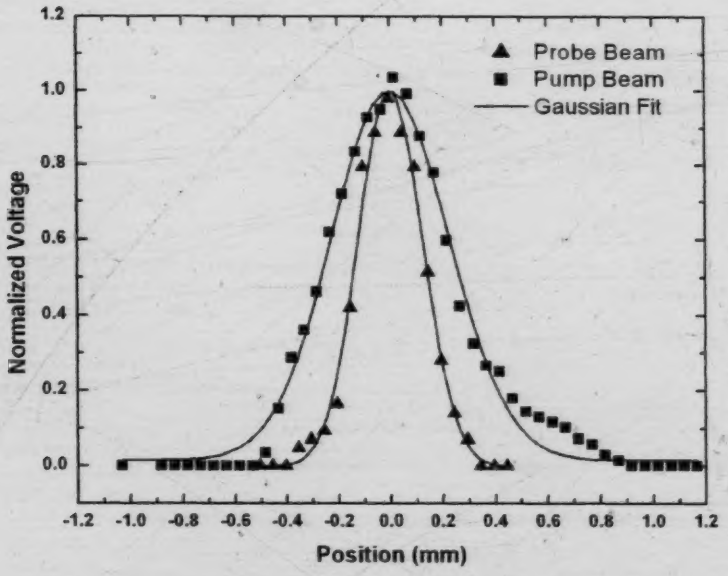

Figure 3.4: Spatial profiles of the pump and probe beams at the sample position.

Another important aspect is the angle between the pump and probe beams at the sample. This angle should be small enough to ensure that they are almost collinear with each other. This strongly influences both the experimental resolution and t0 as will be shown in the following sections.

3.2.2 Determination of Zero Time Delay t_0

The temporal overlap between pump and probe pulses at the sample position was achieved by finding zero time delay, t_0. To find t_0, we projected both beams onto a thick

paper beam block placed at the sample position and observed their arrival times using a silicon photodiode connected to an oscilloscope. By moving the coarse delay stage, we could adjust the probe beam arrival time to overlap with the pump and the course delay stage was fixed at that position. More accurate determination of t_0 was then achieved by placing a quartz slide as a Kerr gate medium at the sample position. We varied the fine delay stage position and observed the Kerr signal in the lock-in. In this configuration, the maximum signal corresponds to a maximum modulation in the probe beam due to the pump beam. The fine delay stage position at this maximum corresponds to t_0. At this stage, the spatial overlap could be further improved by adjusting the pump beam position with the adjustable mirror to maximize the signal. In this way we could determine t_0, which varied slightly when using different bandwidth filters. When comparing Kerr gate signal with transient absorption signals of different samples, we found that the maximum of the Kerr signal overlaps with the half way of the rise (fall) edge of the transient absorption signal (Fig. 3.5).

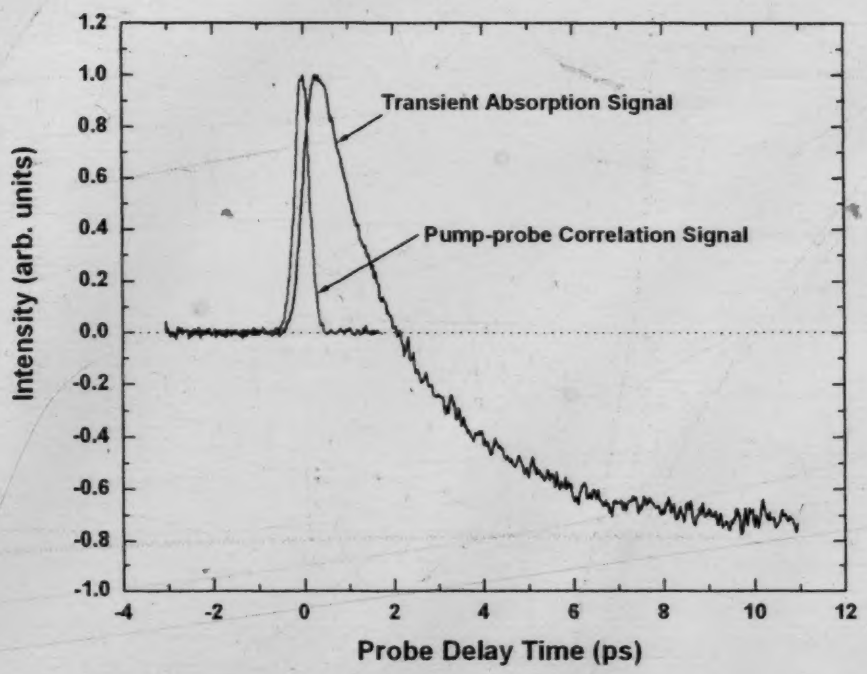

Figure 3.5: Transient absorption signal and pump probe correlation signal obtained by Kerr gate.

3.2.3 Linearity of Detectors

Detecting ultrashort pulses could result in a large number of photons arriving at the photocathode of the detector in a short time. This might result in saturation effects in detectors affecting their linearity (Rulliere 1998). We have tested the Thorlabs PDA100A silicon detectors used in this experiment in the incident intensity range relevant to our measurements by using filtered 630 nm wavelength and confirmed that their response is linear (Fig. 3.6).

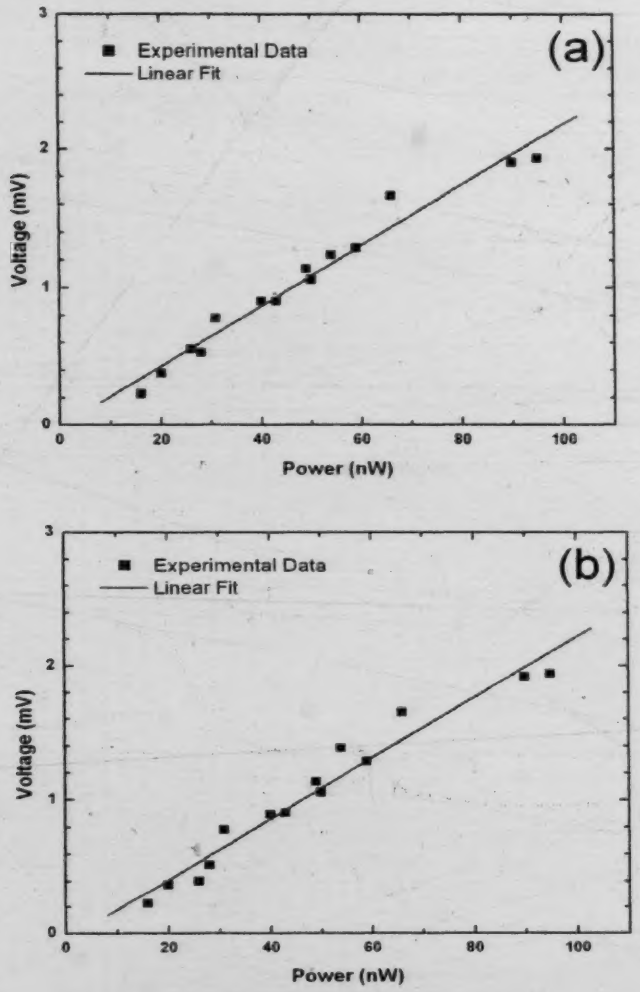

Figure 3.6: Linearity of detector A (a) and detector B (b) for 630 nm wavelength.

3.2.4 Detectors Responsivity

The spectral response of the detectors is non-uniform, as illustrated by their spectral response curve obtained from the manufacturer manual (Fig. 3.7).

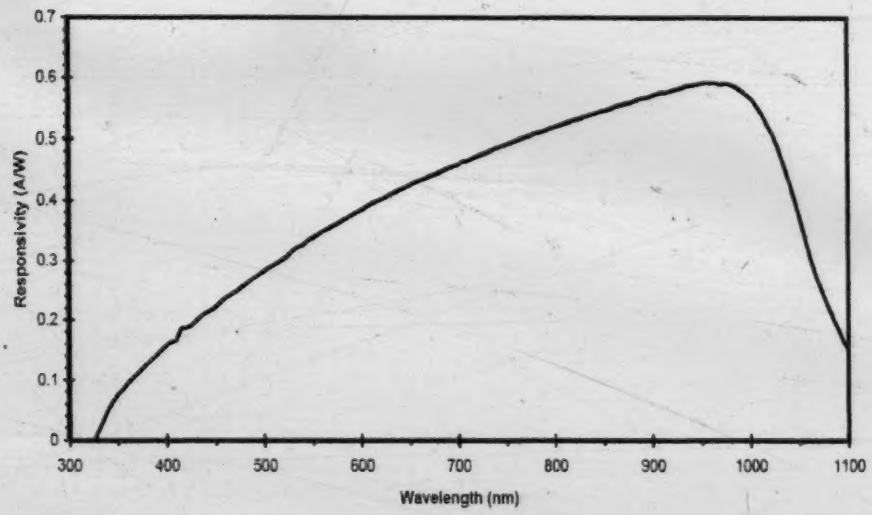

Figure 3.7: Resposivity of the detectors as a function of the wavelength (Thorlabs Catalouge).

In order to overcome this limitation, we used a differential detection technique. With the pump beam blocked, the intensities of the probe beam A and the reference beam B are balanced using neutral density (ND) filters placed before detectors A and B (Fig. 3.1). Both beams are detected by the lock-in amplifiers synced to the 1.08 kHz laser repetition rate. With the detectors balanced in this way, the third lock-in amplifier that monitors the difference A-B detectors give zero background reading in the absence of a pump beam. When the pump beam excites the sample, the probe beam will experience a modulation, and the signals read by detectors A and B will be different. The difference A-B is detected at the frequency of the optical chopper modulating the pump beam, 540 Hz. The signal-to-noise ratio of this technique is very high, estimated at $10^2 - 10^3$. An example of the experimental data is shown in figure 3.8.

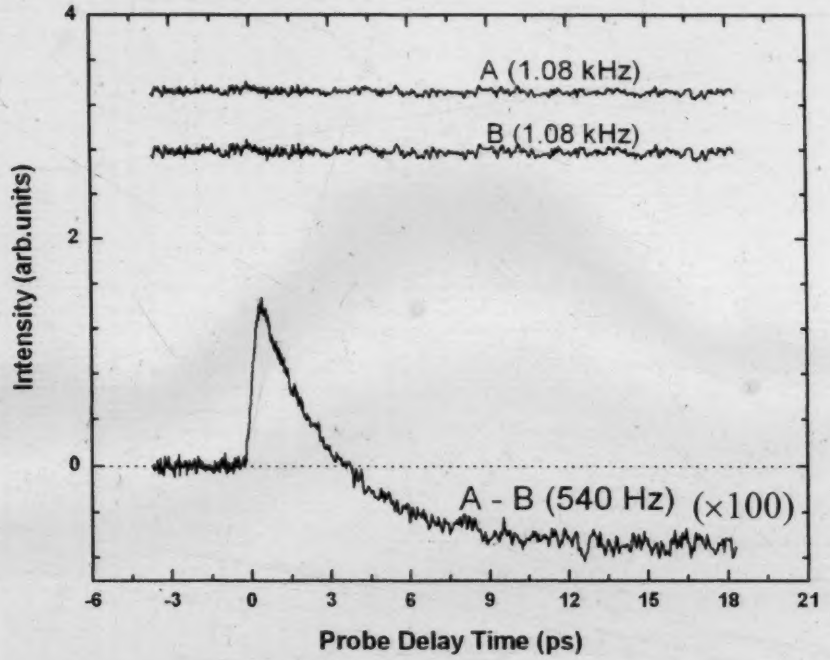

Figure 3.8: Example of the experimental data. Traces A and B are shifted for clarity. Signals A and B were detected with the sensitivity of the lock-ins set to 5 mV, while the sensitivity of the third lock-in monitoring the signal A – B was 50 μV.

The major source of noise in the experiment is the pulse-to-pulse noise of the laser output. The use of a reference beam allows us to significantly reduce the noise in the detected signal. Measuring the A-B signal at 540 Hz further improves the signal-to-noise ratio.

In the data analysis, we calculate the differential signal (A-B)/B which is proportional to the differential transmittance,

$$(A-B)/B \propto (T-T_0)/T_0 \qquad (3.2)$$

Differential detection allows us to eliminate the effects of the non-uniform spectral response of the detectors as well as the wavelength-dependent power variations in the probe beam.

Since the A-B signal is detected at 540 Hz while signal B is detected at 1.08 kHz, the value of (A-B)/B does not reflect the real value of the signal. Therefore, we use the ratio A/B where both A and B signals are detected at 1.08 kHz for calibration of our (A-B)/B signal. Fig. 3.9 shows both A/B and (A-B)/B signals as functions of delay time. The signal A/B has a maximum change of about 10^3 which represents the signal to noise ratio, while (A-B)/B signal is much larger. Fig. 3.9 also illustrates the noise reduction in the measured signal due to differential detection at 540 Hz. Further noise reduction is achieved by taking the average of several successive complete scans. The signal in the example above is an average of three scans.

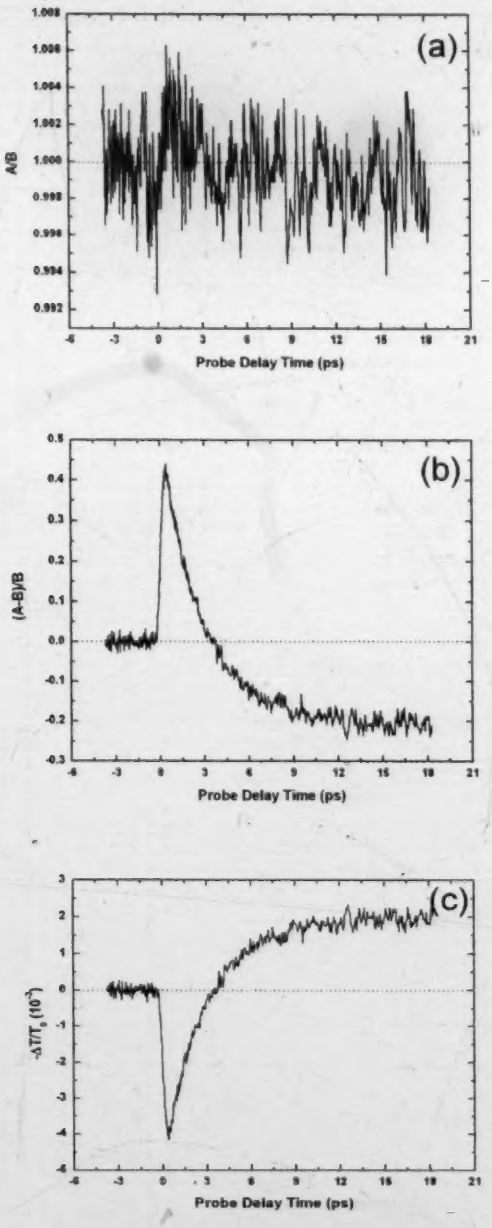

Figure 3.9: (a) The absolute data A/B. (b) The differential data (A-B)/B as a function of the delay time. (c) The calibrated data $-\Delta T/T_0$. This data is the average of three scans.

The A/B signal also provides information about the sign of the transmission change. (A-B)/B is dependent on the lock-in phase and cannot be used to distinguish between the photoinduced enhanced transmission and enhanced absorption. In this particular example, we can see that signal A is larger than signal B at t_0 indicating a pump-induced enhancement in the transmission of the probe beam A comparing to the reference beam B.

4 Characterization of the Experimental Setup

This Chapter discusses the techniques used to test and characterize the experimental setup for the optical pump – probe measurements. A detailed analysis on the influence of the optical components on the temporal duration and chirp is also given.

4.1 Second Harmonic Generation

The 400 nm pump pulses were obtained by second harmonic generation (SHG) in the BBO crystal. The maximum average power of the fundamental 800 nm beam used to generate the 400 nm pulses was 100 mW as measured after the optical chopper. In order to fulfill the phase-matching conditions for SHG, the 800 nm beam was polarized vertically. A conversion efficiency of 15 % from fundamental to second harmonic, which corresponds to an average power of 15 mW for the 400 nm beam, was achieved under these conditions. The resulting 400 nm beam was polarized horizontally.

The blue glass filter placed after the BBO crystal was used to remove the residual fundamental beam. The spectrum of the 400 nm beam after the filter is shown in Fig.4.1, showing the absence of any residual 800 nm beam. Furthermore, no SCG in the BBO crystal is observed. As seen in the inset figure of Fig. 4.1, the spectral envelope of the 400 nm pulses is of typical Gaussian shape centered at (401 ± 1) nm with a FWHM of (3.9 ± 0.1) nm.

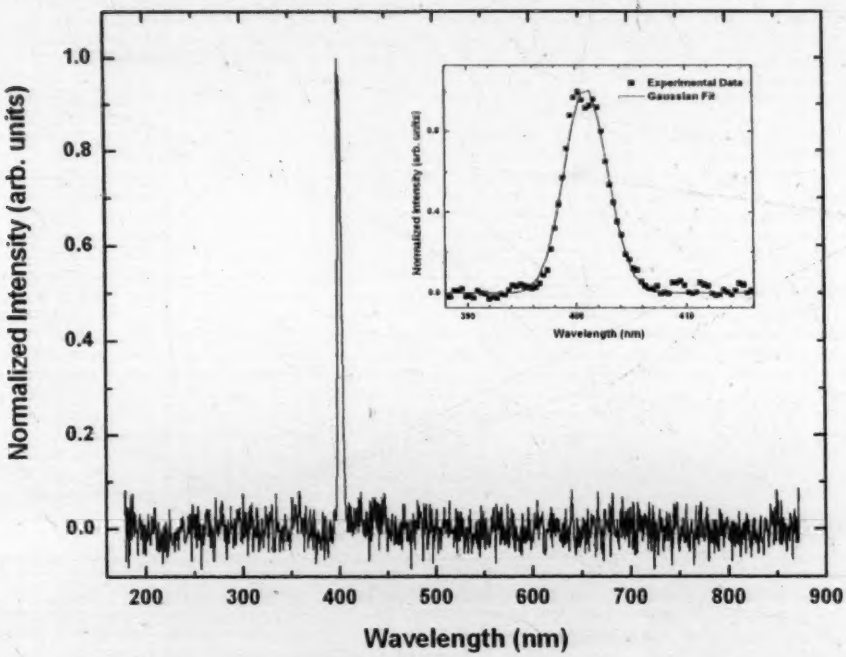

Figure 4.1: The 400 nm pump beam spectrum. Inset: squares – experimental points, curve – Gaussian fit of FWHM of (3.9 ± 0.1) nm.

4.2 Supercontinuum Characterization

SCG was previously established in our lab using 100 fs, 800 nm pulses with an average power of ~100 mW focused by a 30 cm lens into 10 mm quartz water flow cell (Slepkov 2006). The flowing water greatly minimized the fluctuations in SC resulting from air bubbles trapped inside water. In this thesis, we used a generating power of about 25-30 mW focused by a 20 cm lens. In this section, we study the SC used as a probe in the experiments described in this thesis, and discuss its spectral distribution and temporal behavior.

The influence of the generating power on the spectrum and intensity of the white light is shown in Fig. 4.2. The spectrum was collected with an Ocean Optics spectrometer that was calibrated using a tungsten lamp. It is clear that the most intense and spectrally broad supercontinuum is obtained with the highest generating beam power. Therefore, the highest available pump power (25 - 30 mW) was used for the experiments. Spatially, the generated white light continuum consists of a white central part that is collinear with the generating beam surrounded by a conical blue emission. Similar behavior was observed by Brodeur et al., 1996. Such conical emission can be attributed to stimulated parametric four-photon interaction (Xing et al. 1993). The blue conical emission was then spatially filtered by an iris. The spectrum of the white light central part is asymmetric and extends from 400 nm beyond 850 nm (Fig. 4.2). The power of the white light was found to be 17.5 mW when a generating power of 30 mW was used compared to 15mW with a generating power of 25 mW. This indicates almost equal conversion efficiency in this generating power range. It is also clear that most of the power is concentrated around the 800 nm original pulse.

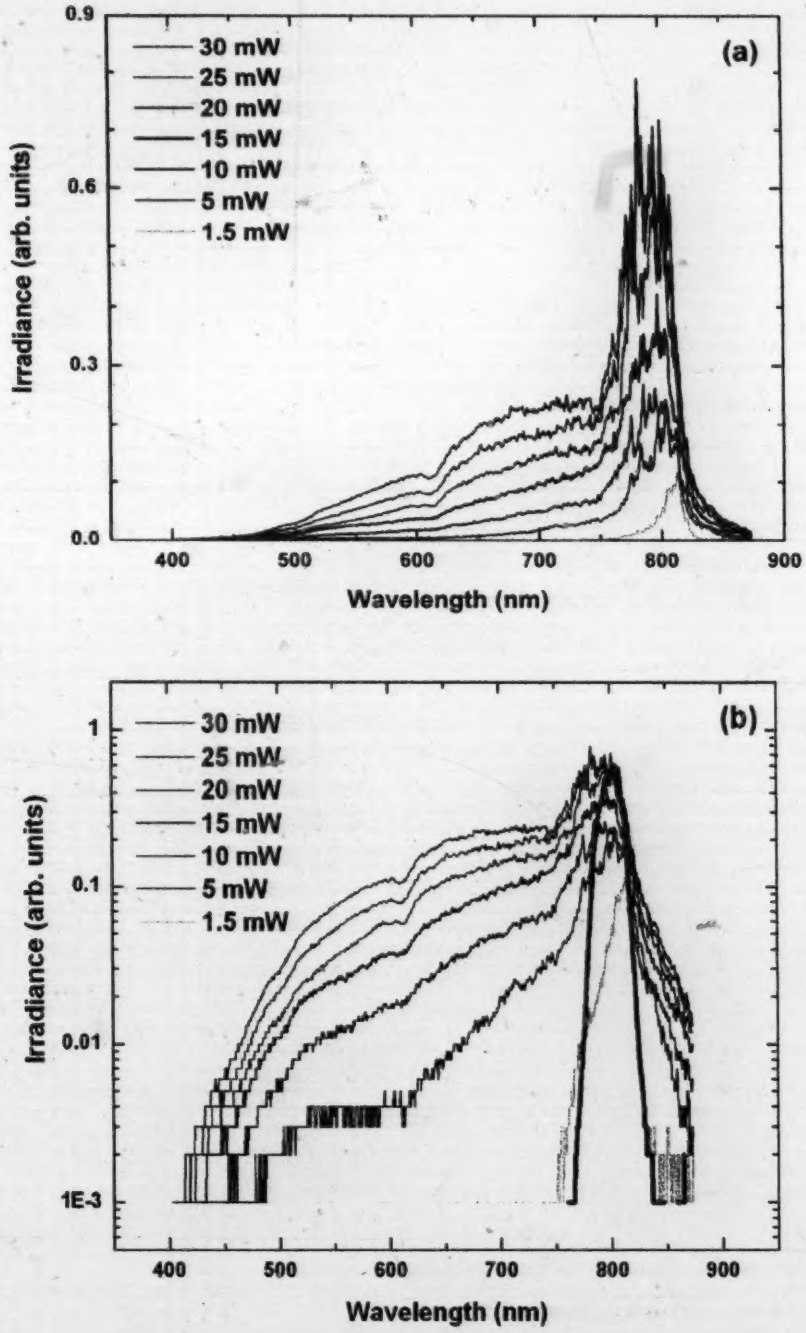

Figure 4.2: SC spectra at different generating powers on a linear-linear scale (a) and on a log-linear scale along with the 800 nm generating beam spectrum (b).

As discussed in Chapter 3, we used narrow band pass filters with 10 nm bandwidth to select wavelengths of the probe beam from the white light continuum. The power losses as the probe beam propagates through the experimental setup are wavelength-dependent, as can be seen in Fig 4.3a. The sudden drop in power as measured before the detectors for wavelength larger than 700nm is caused by the IR cutoff filters that are placed before the detectors in order to eliminate the residual 800 nm beam. The transmission spectrum of the IR cutoff filter is provided in Fig. 4.3b. In order to prevent the residual 400 nm pump beam from effecting the experimental data, a long pass filter with cut-on wavelength 435 nm was used The transmission spectrum of this filter is shown in Fig.4.3c. Because of these filters, our measurements are constricted to the wavelength range from 450 nm to 700 nm. This figure also indicates that the power of the probe beam is sufficient.

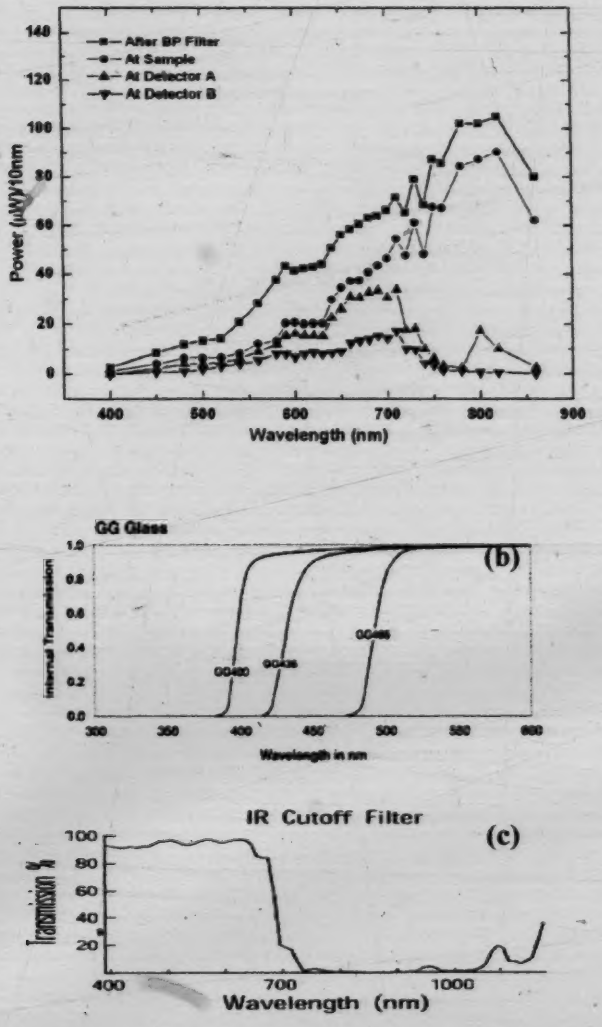

Figure 4.3: (a) SC power at different positions in the experimental setup. Each data point represents the power within 10 nm bandwidth around each probe wavelength as selected by BP filter. (b) Transmission through the 435 nm long pass filter (Thorlabs Catalogue). (c) Transmission through the IR cutoff filter (Edmund Catalogue).

4.3 Pulse Characterization

Characterization of the probe pulses was performed using optical Kerr gate with a quartz slide as the Kerr medium placed at the sample position. Using this method we determined the temporal resolution, duration of pulses, as well as temporal broadening and chirp of the supercontinuum.

4.3.1 Temporal Resolution

The temporal resolution of our experiment was estimated by the FWHM of the cross-correlation of the pump and probe beams at the sample position. The FWHM values were obtained by fitting the experimental data to a Gaussian curve. Typical experimental resolution values were 0.631 ps for 450 nm and 0.318 ps for 700 nm probe pulses.

4.3.1.1 Angle Between Pump and Probe Beams

Angle between the pump and probe was found to affect the resolution of the experiment slightly. Comparison between pump-probe cross-correlation curves taken at two different angles between the pump and probe beams as shown in Fig. 4.4. The FWHM for the curve taken at an angle much smaller than 10° was found to be (0.338 ± 0.001) ps compared to (0.353 ± 0.002) ps at angle larger than 10°. In all of the experiments described in this thesis we kept the angle between the pump and probe as small as possible.

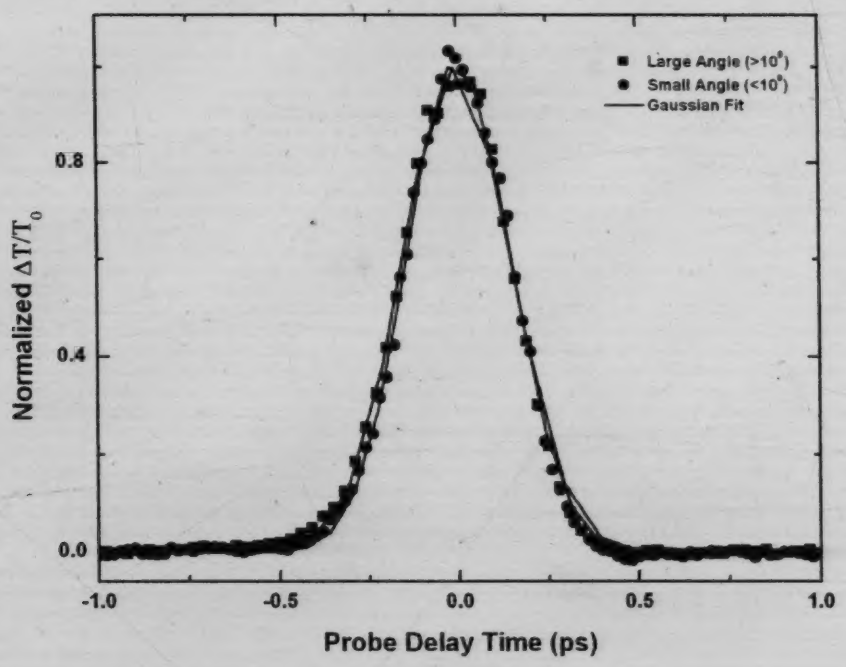

Figure 4.4: The pump-probe cross correlation signal dependence on the angle between the pump and probe beams. The FWHM at angle smaller than 10° is equal to (0.338 ± 0.001) ps compared to (0.353 ± 0.002) ps at angle larger than 10°.

4.3.1.2 Pulse Compressor Setting

The source of the ultrashort 800 nm pulses is an amplified Ti: sapphire laser. Before amplification, the pulses are chirped and temporally stretched in order to reduce the peak power to avoid damaging the system elements. After the gain medium, a compressor comprised of a grating pair is used, which temporally compresses the output pulses. The setting of the compressor *is* an important factor in the temporal resolution of our experimental setup. We have studied the influence of the compressor setting on the efficiency of SHG in the BBO crystal as well as on the total power of the white light continuum. We found that at the compressor setting of 10.5 mm, the powers of the 400 nm pump and of the white light are the highest (Fig. 4.5a). This setting, however, does

not correspond to the shortest pulses as evidenced by the pump-probe cross-correlation measurements (Fig. 4.5b). The data presented in Fig. 4.6 were taken with a probe wavelength of 600 nm. The measurements with 450 nm probe revealed similar results. The relation between pulse duration and SHG and SCG efficiencies needs to be explored in more detail and is out of the scope of this thesis. In this experiment, we chose to set the compressor to 10.5 mm, maximizing the pump and probe powers even though this setting compromises the temporal resolution to a certain degree

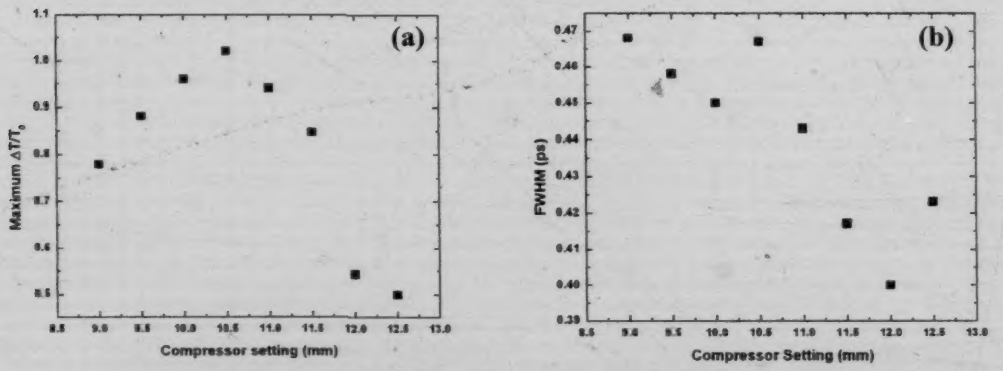

Figure 4.5: Relationship between the compressor setting and the maximum $\Delta T/T_0$ (a) and the FWHM (b) of the pump-probe cross correlation signal.

4.3.2 Temporal Broadening

Propagation of the short optical pulses through the experimental setup components leads to the temporal broadening of the pulses due to the group velocity dispersion. It is crucial to characterize the temporal broadening of the probe pulses due to the optical elements in their path in order to correctly interpret the experimental data.

Using the optical Kerr gate, we studied the pulse duration for different components of white light. First, the autocorrelation of the 800 nm pulse with no water cell or BBO crystal (see Fig. 4.6) was measured in order to estimate the pulse width for the 800 nm pulse for use in the subsequent calculations. Using the FWHM of the correlation signal

which was equal to (109 ± 1) fs and the decorrelation factor γ obtained from Fig 2.4, we obtained pulse duration of about (89 ± 1) fs.

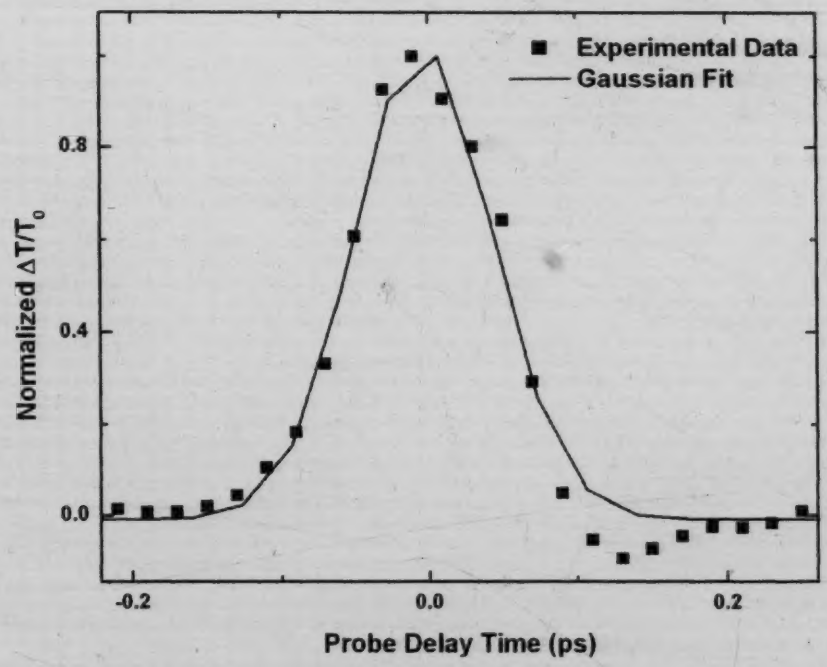

Figure 4.6: 800nm-800nm autocorrelation signal with FWHM of (109 ± 1) fs.

To estimate of the duration of the 400 nm pump pulses, we measured the cross correlation between the 400nm and the 800 nm beams as shown in Fig.4.6. The FWHM of this correlation is (230 ± 9) fs. As this value is significantly larger than that of the 800-800 nm autocorrelation signals, we assume that the duration of the 400nm pulse is equal to the correlation signal FWHM, (230 ± 9) fs. This indicates a substantial broadening of the pulse in the second harmonic generation crystal and the blue glass filter used to block the residual fundamental beam.

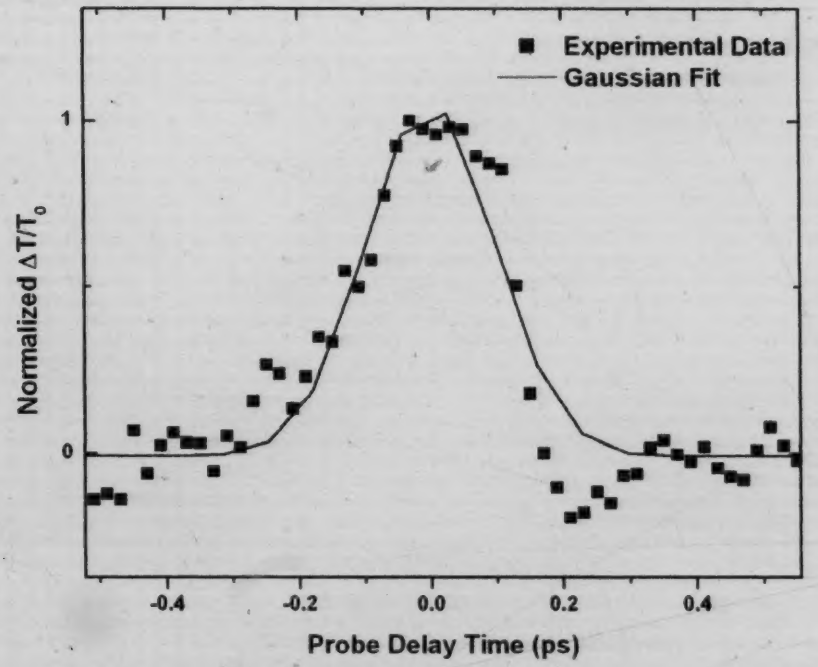

Figure 4.7: 400nm-800nm cross correlation signal with FWHM of (230 ± 9) **fs.**

Using the pulse duration obtained for the 400 nm beam and correlating this beam with the different probe wavelengths, the duration of the probe pulses, Δt, and their time bandwidth products, which was calculated assuming 10 nm pulse bandwidth, at each wavelength could be obtained and the results are presented in table 4.1.

λ (nm)	τ_{FWHM} (ps)	γ	Δt (ps)	$\Delta\nu$ (10^{13}Hz)	$\Delta t\Delta\nu$
450	0.631±0.007	1.03±0.02	0.613±0.005	1.48±0.2	9.08±0.07
480	0.458±0.006	1.06±0.02	0.432±0.002	1.30±0.2	5.63±0.03
520	0.388±0.005	1.08±0.02	0.359±0.002	1.12±0.2	3.98±0.02
580	0.445±0.004	1.06±0.02	0.420±0.004	0.89±0.2	3.75±0.03
600	0.390±0.006	1.07±0.02	0.364±0.001	0.83±0.2	3.03±0.01
630	0.434±0.006	1.06±0.02	0.409±0.002	0.76±0.2	3.09±0.02
650	0.361±0.008	1.09±0.02	0.331±0.001	0.71±0.2	2.35±0.01
680	0.381±0.005	1.09±0.02	0.350±0.002	0.65±0.2	2.27±0.01
700	0.318±0.008	1.15±0.02	0.277±0.002	0.61±0.2	1.70±0.01

Table 4.1: Values of the FWHM of different pump probe cross correlation signal, the corresponding decorrelation factor γ, the corresponding probe pulse duration, Δt, and the pulse duration-bandwidth product obtained for the duration of the probe pulses at different wavelengths.

For all probe wavelengths, values obtained for the FWHM for the pump-probe cross correlation are larger than the temporal duration of the pump pulse. Therefore, the assumption that the gating pulse is shorter than the probe pulse is valid. Since $\Delta t\Delta\nu >$ 0.441 as seen in table 4.1, the pulses are not transform limited.

From the probe pulse duration, the pulse broadening was calculated assuming initial pulse duration of 89 fs. The temporal broadening at different probe wavelengths is plotted in Fig. 4.8.

Theoretical temporal broadening resulting from the group velocity dispersion in the water cell and other optical elements between the water cell and Kerr medium can be calculated using the material parameters and geometrical dimensions of the optical elements. Detailed calculations are presented in Appendix A. These calculations assumed that the supercontinuum is generated in the first mm of the water cell. The temporal broadening of the probe pulses of different central wavelengths in various optical elements as well as the resulting total temporal broadening is plotted in Fig. 4.8. As is clear from Fig. 4.8, the experimentally determined broadening is comparable to the calculated one.

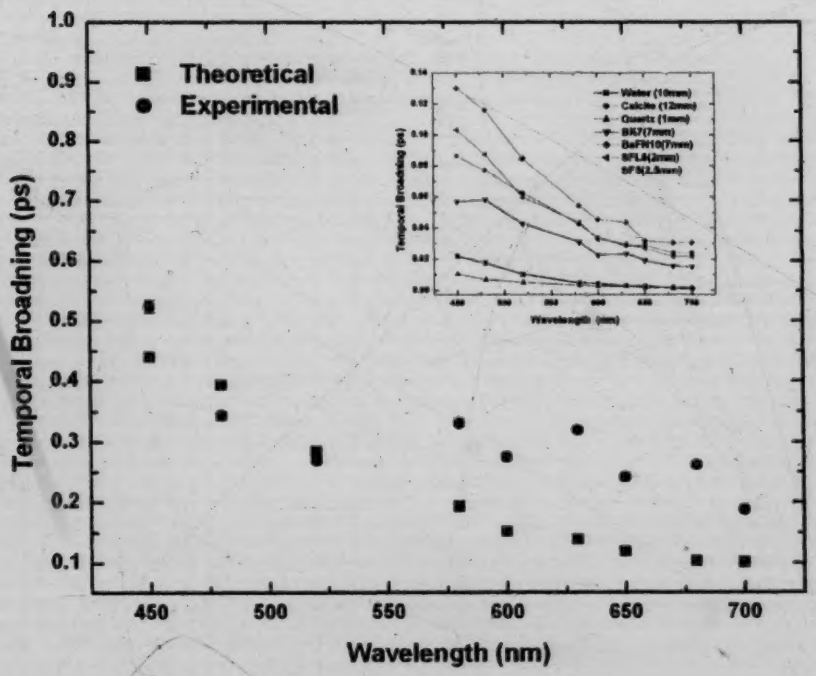

Figure 4.8: The total temporal broadening obtained experimentally compared to the one calculated using the theoretical GVD. Inset: Calculated temporal broadening for the various optical elements.

4.3.3 Chirp

Based on the measured correlation spectra, the relative arrival delay times of the probe pulses with different central wavelengths at the sample position with respect to the 450 nm pulse arrival time were determined. It was observed that the shorter wavelengths are delayed with respect to the longer wavelengths. The theoretical arrival time of the peak of each probe was calculated taking into account GVD in different optical elements using equation 2.11 and plotted in Fig 4.9. Details of the calculation are shown in Appendix A. It is clear from the comparison of the measured and calculated delay times that this chirp in the white light continuum pulses is caused by the group velocity dispersion in the water cell as well as optical components between the water cell and the sample.

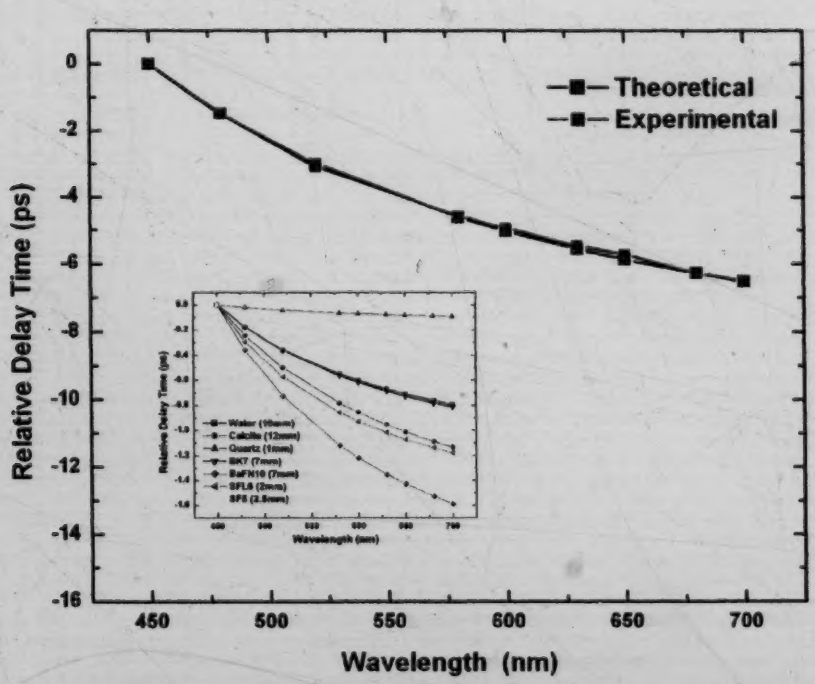

Figure 4.9: The relative delay time obtained experimentally for different wavelengths compared to the expected one from GVD. Inset: Relative delay time expected from each optical components.

5 The Study of Nanostructured Silicon Thin Films

5.1 Silicon Thin Films

5.1.1 Sample Preparation

Amorphous silicon (a-Si) and polycrystalline silicon (pc-Si) thin films on quartz substrates were prepared by the group of Dr. Al Meldrum. First, silicon films with thicknesses of 5, 10, 15, 20, 25, 30, 40, 50, 60, 80 and 100 nm (Fig. 5.1) were deposited on a quartz substrate by electron beam evaporation. The variation in thickness was achieved by a sliding shutter with a moving step of a quarter inch. This formed a-Si films at room temperature. The sample was then cut into two halves along the thickness-changing direction. One of the halves was then annealed at 800 $^{\circ}$C in flowing N_2 gas for a period of one hour. Such annealing temperature was found to crystallize a-Si and forms pc-Si films (Lioudakis et al. 2006, Cooke 2007). The other half was left as deposited. Colors of the films varied widely for different thicknesses. Moreover, the colors of polycrystalline and amorphous films of the same thickness also differed (see Fig. 5.1).

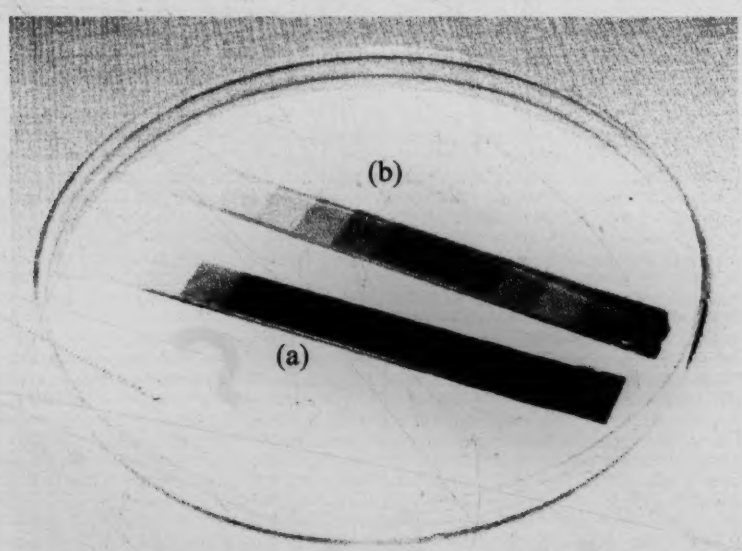

Figure 5.1: (a) Amorphous silicon films (b) Polycrystalline silicon films.

5.1.2 Transmission Spectra

The transmission spectra for these samples were obtained using an Ocean Optics spectrometer and a tungsten light source (Fig 5.2). The transmission of the quartz substrate was used as a reference. Multiple interference effects were observed in the transmission spectra of the a-Si and pc-Si films of the largest thicknesses, as evidenced by the periodic modulation of the spectra. Such behavior arises from reflections from air-silicon and silicon-substrate interfaces. This behavior has important influence on the photoinduced transmittance obtained in a pump probe experiment.

In this case, the photoinduced change in transmission is equal to (Shkrob and Crowell 1998)

$$\Delta T \approx (\frac{\partial T}{\partial n})\Delta n + (\frac{\partial T}{\partial \kappa})\Delta \kappa, \qquad (5.1)$$

where Δn and $\Delta \kappa$ are the photoinduced changes in refractive index and extinction coefficient, respectively as discussed earlier in section 1.3.

Annealing was found to enhance the contrast in the interference fringes. Furthermore, high temperature annealing had a more pronounced effect on the transmission spectra of thicker films compared to the thinner films.

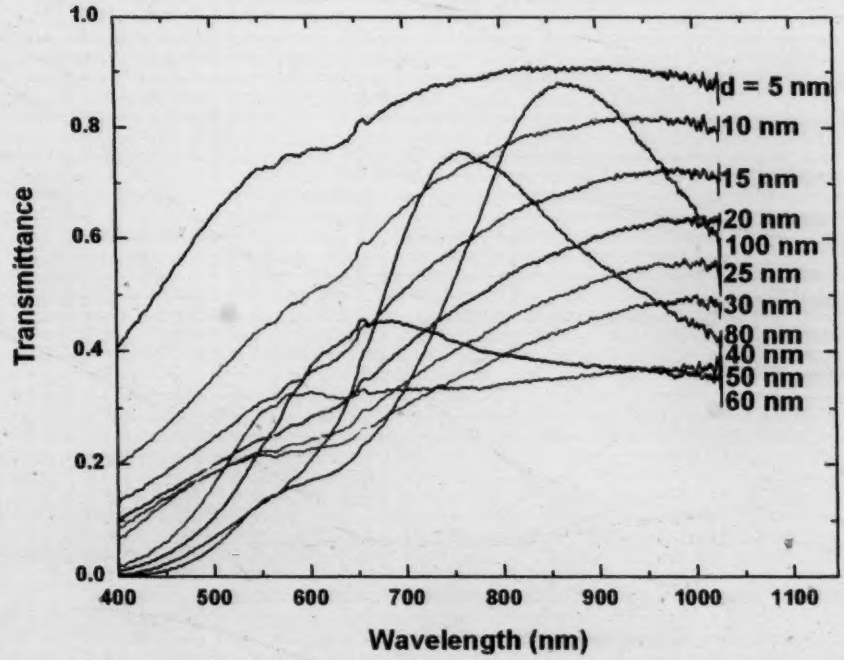

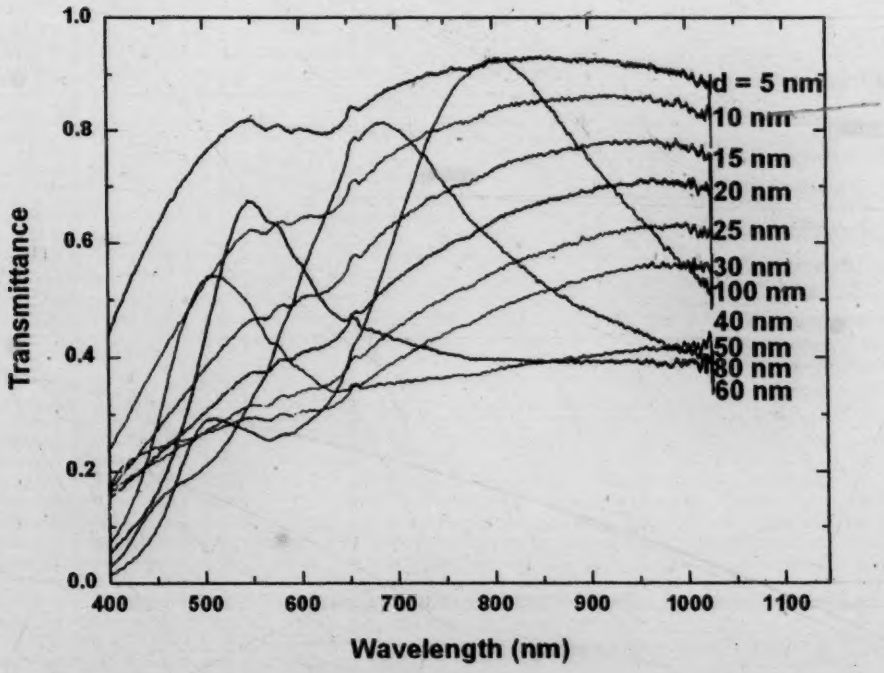

Figure 5.2: Transmission spectra of a-Si (a) and pc-Si (b) films at different wavelengths.

5.1.3 Ultrafast Carrier Dynamics

5.1.3.1 Effect of Annealing

In order to investigate the differences in carrier dynamics in amorphous and polycrystalline Si films, we performed the transient absorption measurements of the a-Si and pc-Si films of the same thickness (100 nm) and same incident pump fluence (0.54 mJ/cm^2) using different probe wavelengths. The resulting negative differential transmission curves are shown in Fig. 5.3.

In the case of a-Si films, the transient absorption of all probe wavelengths experiences a rapid initial rise with no recovery within the studied time range. Similar behavior of the transient absorption was observed by Fauchet *et al.* 1986 in a-Si:H probed with photons of energy larger than the band gap. It was attributed to the fact that for probe wavelengths above the gap, both interband and intraband absorption coefficients remain almost unchanged. The long-lived absorption was found to originate from band gap renormalization due to the increase in lattice temperature. This results in a reduction of the energy gap, which in turn results in a red shift in the absorption curve. This behavior can be used to distinguish between electronic and lattice contributions to the transient absorption signal depending on the probing wavelength (Tanguy et al. 1988). The behavior of the transient absorption observed in our a-Si sample is consistent with these observations since all the probe energies are larger than the band gap of E_g = 1.5 eV (Esser et al. 1990).

Unlike the amorphous film, the behavior of the transient absorption in the annealed film varies dramatically depending on the probe wavelength. At 450 nm, no recovery of the photoinduced absorption was observed in the studied time range. At 500 nm, transient absorption showed a very slow recovery. This behavior is similar to that of the amorphous sample, and can be explained by the fact that short wavelengths probe are more sensitive to lattice heating rather than electronic behavior (Downer and Shank 1986). At 634 nm and 700 nm, a faster response occurs at early times following the pump pulse compared to photoinduced absorption observed at short pump wavelength. This

fast response can be attributed to the photoinduced carriers response. This fast relaxation continues at a slower rate in the positive side of the curve due to the heating of the lattice. This lattice heat is observed to relax at a very slow rate to equilibrium.

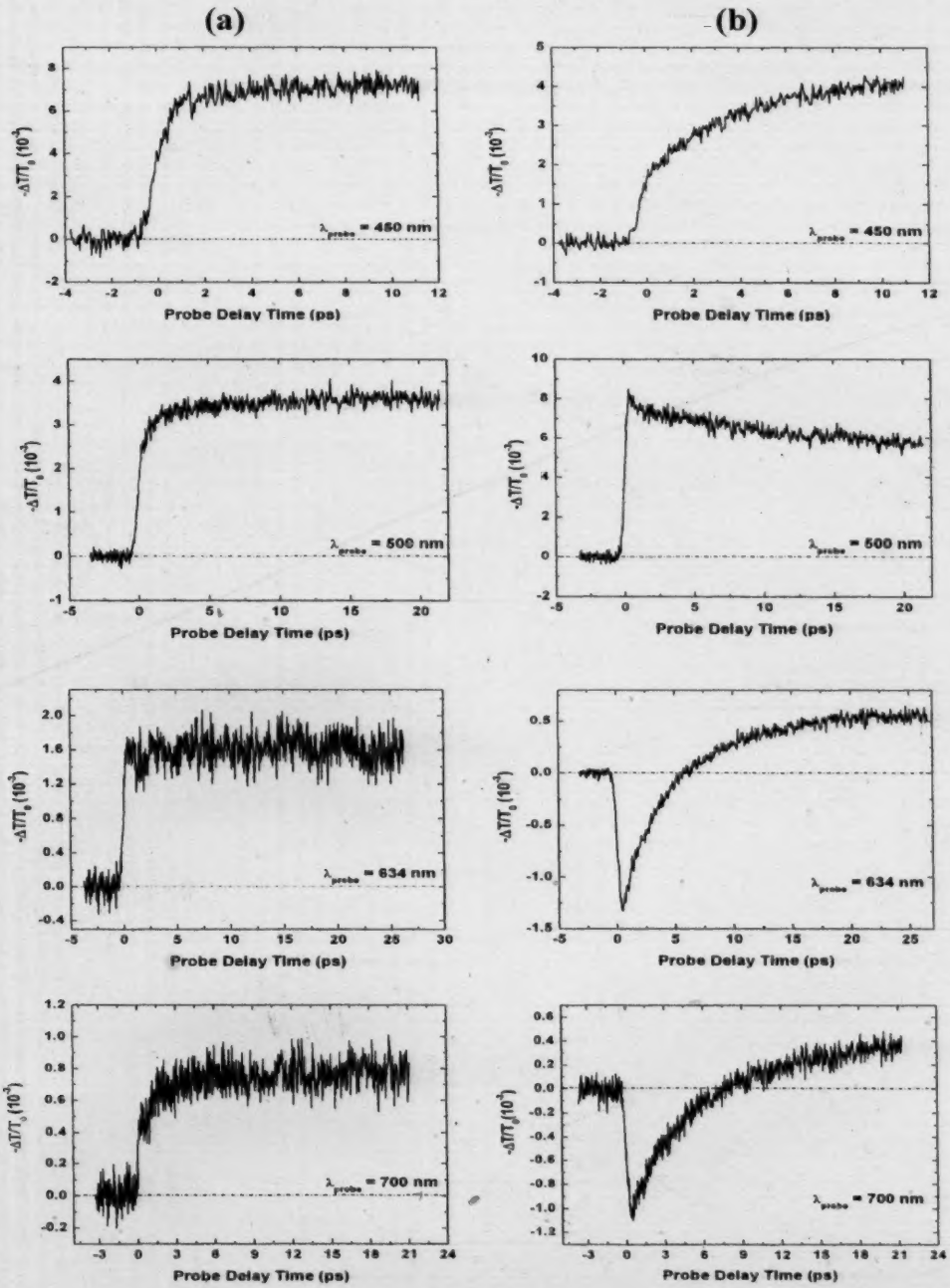

Figure 5.3: Time resolved differential transmittance signals at different probe wavelengths for a-Si (a) and pc-Si (b) for film thickness of 100 nm and incident pump fluence of 0.54 mJ/cm^2.

5.1.3.2 Thickness Dependence

In order to investigate the dependence of the ultrafast carrier dynamics on thickness of the sample, we studied the pc-Si films (annealed samples) with different thicknesses at same incident pump fluence (0.82 mJ/cm^2) and same probe wavelength (630 nm) as shown in Fig. 5.4. For the samples with thicknesses in 10 nm to 40 nm ranges, the transient absorption curves appear similar. These samples demonstrate enhanced transmission at early times after the pump pulse, followed by a relaxation towards equilibrium and a subsequent increase in absorption. The transient absorption signal for the 50 nm and 60 nm samples looks remarkably different: photoinduced absorption is observed at early times instead of the enhanced transmission. For samples with thickness above 60 nm, enhanced transmission is recovered. These striking variations in the signal can be explained based on wavelength-dependent photoinduced changes in refractive index and extinction coefficient. We have examined the transmission spectra of the pc-Si films of different thicknesses in Fig. 5.2 at the probe wavelength of 630 nm over 10 nm bandwidth. Due to interference fringes, the slopes of these spectra can be positive or negative. These have an effect on the measured photoinduced absorption as found earlier by Downer and Shank, 1986 as can be seen in Fig. 5.5. In the times immediately after excitation, the presence of the photoexcited free carriers leads to a decrease in refractive index (see Eq. 1.5) and an increase in absorption. The negative change in refractive index blue shifts the interference fringes and the positive change in absorption shifts the transmission curve downwards (Fig. 5.5). In this figure, there is no enhanced transmission due to the large change in absorption compared to the change in refractive index. However, if the change in refractive index is more prominent, the blue shift can lead to enhanced transmission in the rising edge of the fringes and more absorption in the falling edge of the fringes. Although this was not stated in literature to our knowledge, it agrees well with our transmission spectra. For the samples with thicknesses in 10 nm to 40 nm and 80 nm to 100 nm ranges, the transmission at 630 nm lies in the rising edge of the interference fringes. Therefore, we expect the blue shift caused by the decrease in refractive index to result in increase in the differential transmission signal.

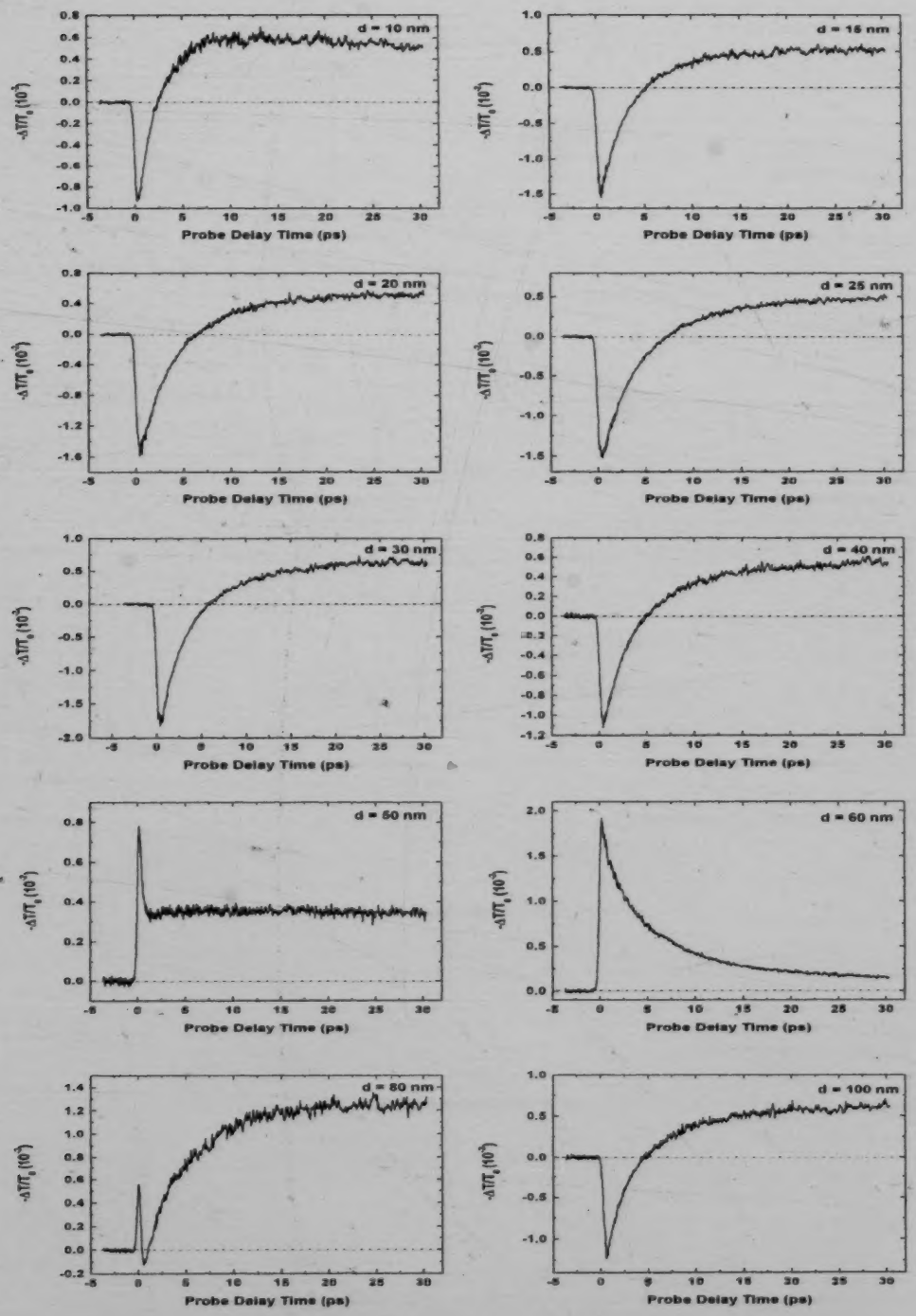

Figure 5.4: Time resolved differential transmittance signal for different film thicknesses of pc-Si at pump fluence of 0.82 mJ/cm^2 and λ_{probe} = 630 n m.

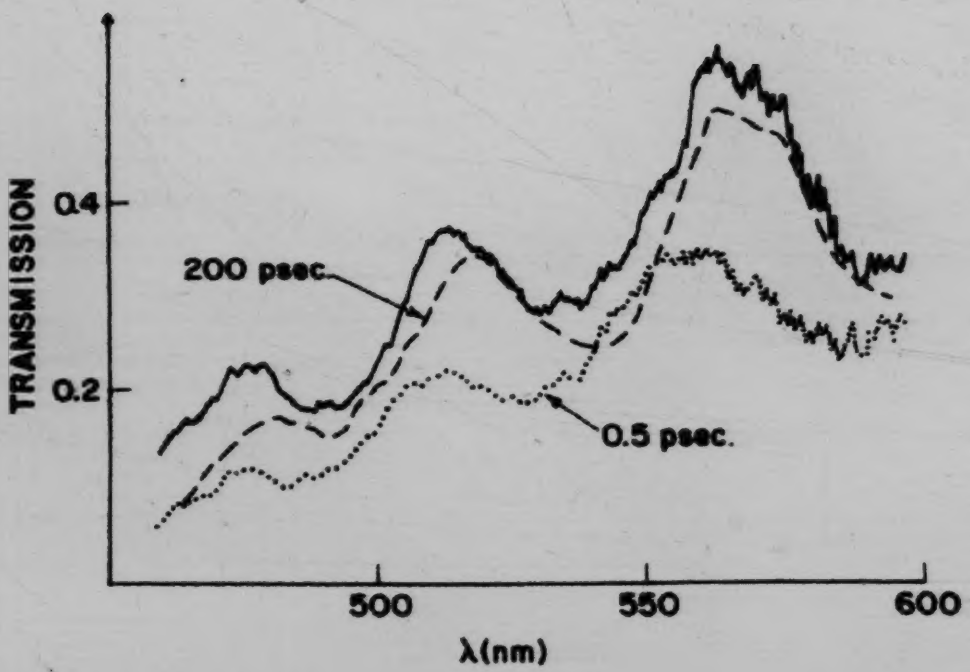

Figure 5.5: The transmission spectra of 0.5 μm silicon on sapphire film before excitation (solid curve), at probe delay times of 0.5 ps and 200 ps. At 0.5 ps, there is a blue shift of fringes and a strong absorption caused by the presence of dense electron hole plasma. At 200 ps, there is a red shift caused by lattice heating (Downer and Shank 1986).

On the other hand, for sample thicknesses of 50 nm and 60 nm, the probe wavelength of 630 nm lies on the falling edge of the fringes, which leads to a decrease in the transmission of the probe beam at early times.

At later times, the free carriers relax to equilibrium and recombine, the absorption of the probe beam decreases. At the same time, the temperature of the crystal lattice rises because of the energy released by the relaxed photoinduced carriers, resulting in an increase in the refractive index and absorption. The positive change in refractive index leads to red shift in the transmission curve. If the change in absorption in this case is more prominent than the change in refractive index, we expect to get enhanced absorption in both the rising and falling edge of the interference fringes. This is evident in all sample thicknesses, which demonstrate absorption that does not change to enhanced transmission at longer times. Quantitative measurements using Eq. 5.1 and measuring the refractive index from differential reflectivity should be done to check those analyses.

5.1.3.3 Probe Wavelength Dependence

In order to study the influence of the probe wavelength on ultrafast carrier dynamics, we performed transient absorption measurements on 10 nm thick pc-Si film at same pump fluence (0.68 mJ/cm^2) and different probe wavelengths. The resulting data are shown in Fig.5.6a.

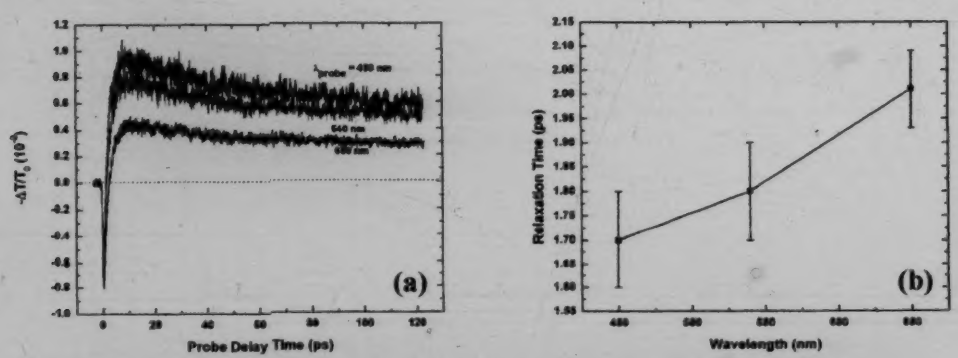

Figure 5.6: (a) Time resolved negative differential transmittance spectra at different probe wavelength for the 10 nm pc-Si film and incident pump fluence of 0.68 mJ/cm^2. (b) The carrier relaxation time as a function of the probe wavelength.

At all wavelengths, we observed an initial enhanced transmission, followed by an increase in absorption and its subsequent recovery as carriers relax to equilibrium. When fitted to single exponential function, the relaxation of the enhanced transmission was found to be slower at longer probe wavelengths (Fig.5.6b). Similar behavior was observed in highly implanted and annealed pc-Si films (Lioudakis et al., 2005).

At the later times, we observed increase in absorption above the initial value. The maximum value was wavelength-dependent, with shorter wavelengths exhibiting larger absorption. This result is in agreement with the previous findings that the red shift in transmission curve due to lattice heating is more pronounced at shorter probe wavelengths (Fig. 5.5), and therefore results in larger increase in absorption, compared to longer wavelengths.

5.1.3.4 Pump Fluence Dependence

We have also studied the pump fluence dependence of ultrafast carrier dynamics. Photoinduced transient absorption measurements were performed on the 10 nm thick pc-Si sample with the probe wavelength 600 nm and varying fluence of the pump beam. Figure 5.7a shows examples of the transient absorption spectra at four different pump fluences. The absolute maximum negative differential transmittance signal as a function of the pump fluence is plotted in Fig.5.7b. At low pump fluences, the maximum change in signal increases linearly with pump fluence from the zero point. At pump fluences larger than 1 mJ/cm^2, the maximum change in transient absorption continues to grow but with a different slope and a vertical offset. This offset is likely caused by the residual signal that exists at high pump fluences and results in a signal even when the probe pulse precedes the pump pulse. For details, see Appendex B.3.

Using penetration depth of $\delta = \frac{1}{\alpha} = 82$ nm for $\lambda = 400$ nm in crystalline silicon (Palik 1998), the initial carrier density was calculated for different pump fluences using Eq. 1.2. The carrier relaxation time was determined by fitting the relaxation part of the transient

absorption signal to the single exponential function. The resulting carrier relaxation times as a function of initial carrier density are plotted in Fig. 5.7c. The relaxation time is independent of the initial carrier concentration at low carrier densities. However, in the high carrier density ($>1\times10^{20}cm^{-3}$) region the relaxation time decreases with the increasing carrier density. This behavior is indicative of the carrier density dependant Auger recombination.

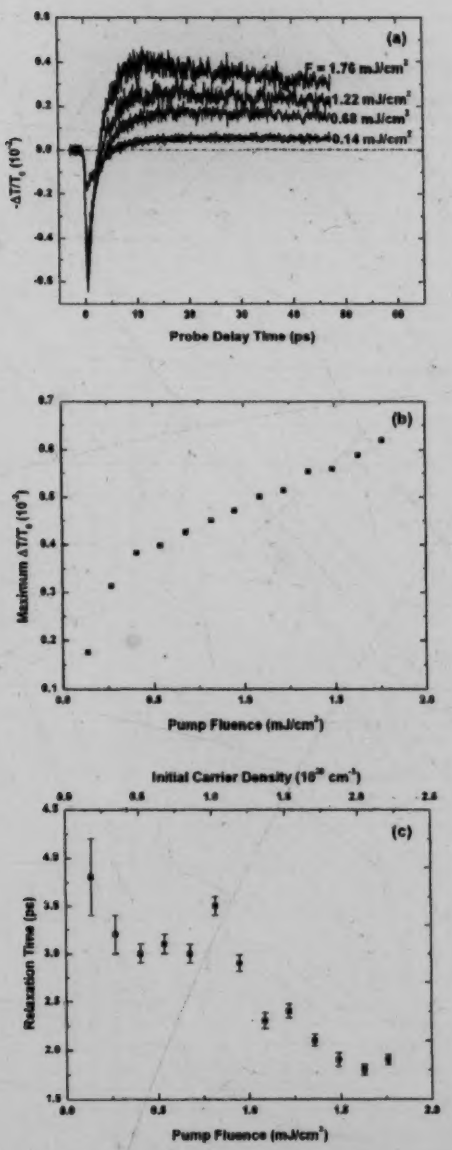

Figure 5.7: (a) Examples of negative differential transmittance spectra at different pump fluence. (b) Maximum absolute change of negative differential transmittance. (c) Measured photoinduced carrier relaxation time at different pump fluence as a function of carrier density.

5.2 Silicon Nanocrystal Thin Film

5.2.1 Sample Preparation

The Si nanocrystal film was prepared by the group of Dr. Al Meldrum. Approximately 1.3 μm thick $SiO_{1.5}$ film was synthesized by simultaneous electron beam deposition of SiO_2 and thermal evaporation of SiO with same deposition rates onto quartz substrate. To initiate the formation of silicon nanocrystals, the film was annealed at 1000 °C in flowing mixture of 95% N_2 and 5% H_2 for a period of one hour. This sample demonstrated a photoluminescence (PL) peak around 725 nm as shown in Fig.5.8. The broad width of the PL spectrum is due to the size distribution of silicon nanocrystals that gives rise to the variation in energies of the defect-related and surface electronic states involved in radiative recombination.

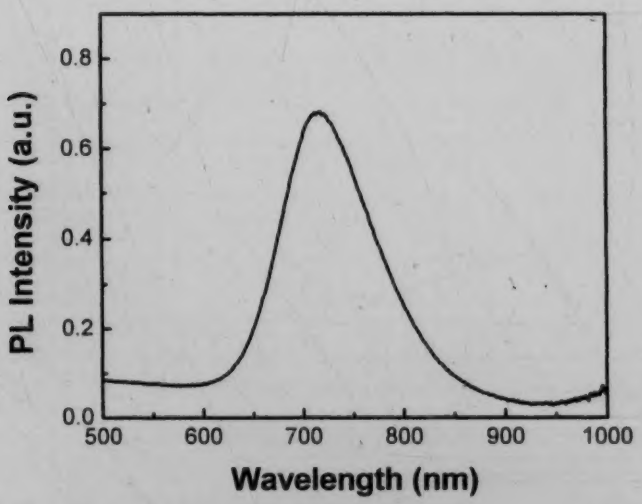

Figure 5.8: Photoluminscense spectrum of the silicon nanocrystal silicon film. Excited with both 325 nm and 442 nm CW laser lines.

5.2.2 Ultrafast Carrier Dynamics in Si Nanocrystal Film

5.2.2.1 Probe Wavelength Dependence

In order to study photoinduced carrier dynamics, we measured transient absorption in the nanocrystal thin film with the different probe wavelengths at a pump fluence of 0.40 mJ/cm^2. The resulting data are shown in Fig. 5.9. For all probe wavelengths, we observed a pulse limited fast rise in negative differential transmittance signal followed by a slow decay. The initial increase in this signal coincides with the pump - probe pulse cross correlation suggesting that it originates from photoinduced free carrier absorption. Photoexcited free carriers absorb the photons of the probe pulse and couple to the higher energy levels. The maximum negative transmittance signal increases at longer probe wavelengths due to the increasing density of states as the probe wavelength approaches the peak PL wavelength of 750 nm.

As can be seen from Fig. 5.9b and 5.9c, the subsequent relaxation of the free carriers follows a biexponential decay

$$A_1 e^{-\Delta t/\tau_1} + A_2 e^{-\Delta t/\tau_2} + A_3, \qquad (5.2)$$

where τ_1 and τ_2 are the relaxation time constants, A_1 and A_2 are the amplitudes of the first and second terms and A_3 is a constant offset. This indicates the presence of two different relaxation mechanisms. Both the fast and slow decay time constants become smaller with increasing probe wavelength. The fast decay time constant ranges from (0.52 ± 0.09) ps for 600 nm to pulse width limited decay for 700 nm. The slow decay time constant decreases from (6.1 ± 0.9) ps for the probe wavelength of 600 nm to (4.8 ± 0.3) ps for 700 nm. Similar behavior was observed by Lioudakis *et al.*, 2007 and Klimov *et al.*, 1998 in contrast to the stretched exponential decay that was observed by Cooke *et al.* 2006 and Cooke *et al.* 2007. Dependence of the relaxation times on the probe wavelength indicates that different wavelengths probe different energy states. The

fast relaxation mechanism could be attributed to the relaxation of the interface states, while the slow relaxation mechanism could correspond to relaxation of carriers in the quantized energy levels in silicon nanocrystals.

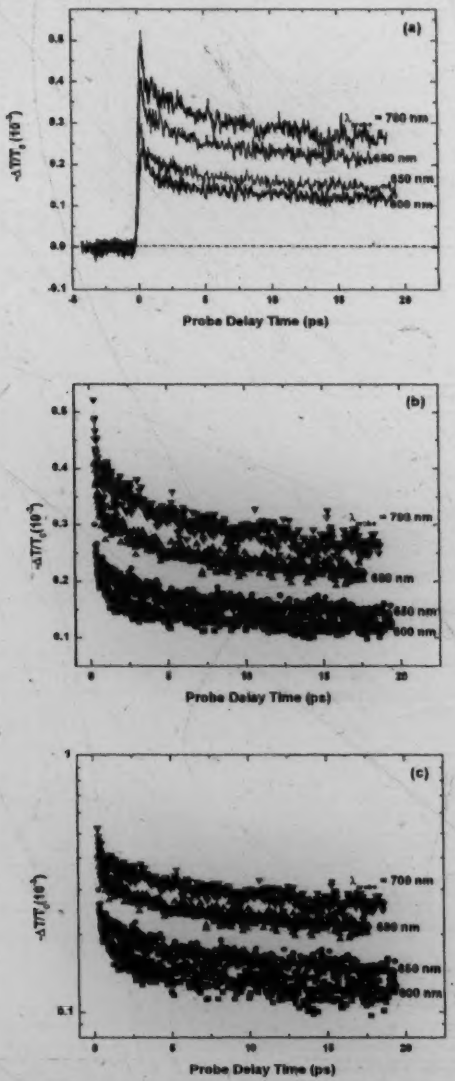

Figure 5.9: (a) Time resolved negative differential transmittance signal in the silicon nanocrystals film at different probe wavelengths and incident pump fluence of 0.40 mJ/cm^2 (b) The relaxation of the negative differential transmittance is fit to biexponential decay function. (c) The same decay is plotted on a log-linear scale.

5.2.2.2 Pump Fluence Dependence

As in the case of the pc-Si film, the dependence of photoexcited carrier dynamics in Si nanocrystal film on the pump fluence was explored at a fixed probe wavelength of 634 nm. The sample negative differential signals at different pump fluences are shown in Fig. 5.10a. These spectra reveal pump fluence and therefore initial carrier density dependence of carrier dynamics. Such behavior was observed in a similar silicon nanocrystals system (Maly et al. 2007) and in other silicon nanocrystals systems such as hydrogenated nanocrystalline silicon (Myers et al. 2001), and colloidal silicon nanocrystals (Bread et al. 2007). The negative differential transmission at early times after the pump pulse ($0.3ps$) as well as at later times ($16ps$) as a function of the pump fluence is plotted in Fig. 5.10b. It was found that the magnitude of negative transmittance at early times ($0.3ps$) scales quadratically as a function of pump fluence as shown in Fig. 5.10b. Similar observation was made by Maly *et al* in the fast photoluminescence dynamics of silicon nanocrystals (Maly et al. 2007). It was explained by the Auger recombination of carriers in nanocrystals containing two photoexcited electron-hole pairs. On the other hand, the magnitude of the negative differential transmittance at $16ps$ was found to have linear dependence on the pump fluence.

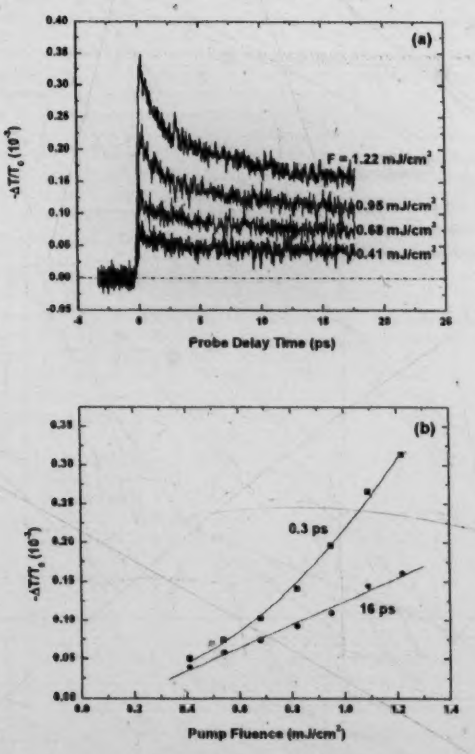

Figure 5.10 (a) Time resolved negative differential transmittance signal at different pump fluences. (b) The negative differential transmittance amplitude at 0.3 ps and 16 ps probe delay times.

6 Conclusions and Future Directions

The objective of this thesis was twofold: to construct and characterize an optical pump supercontinuum probe experimental setup, and to use this setup to investigate ultrafast carrier dynamics in nanostructured silicon films. The developed PSCP setup provided both wavelength tunibility from 450 nm to 700 nm and subpicosecond time resolution.

Ultrafast transient absorption measurements were performed on three different types of nanostructured silicon thin films: amorphous silicon, polycrystalline silicon and nanocrystal silicon films. The dependence of carrier dynamics on various parameters such as annealing temperature (and therefore, crystallinity of the film), film thickness, probe wavelength and pump fluence were studied.

In order to study the effects of the high temperature (800^0C) annealing on the silicon thin film properties, we compared properties of as-grown and annealed thin films of varying thickness. The as-grown silicon films are amorphous, and annealing them at temperatures $\geq 800^0$C leads to the formation of the polycrystalline silicon films. The study of the transient absorption in the amorphous silicon films demonstrated that photoexcited carrier dynamics is independent of the probe wavelength, exhibiting fast initial rise of the photoinduced absorption with no appreciable recovery within the investigated time range. The long photoinduced absorption recovery time is explained by the band gap renormalization due to heating of the lattice by the relaxing carriers. The observed independence of the carrier dynamics on the probe wavelength can likely be explained by the limited wavelength range available in the current experimental setup that prevented us from probing carriers in the extended band tail of amorphous silicon.

Annealing of amorphous silicon at 800^0C to form polycrystalline silicon films had a dramatic effect on the carrier dynamics. Unlike the amorphous films, carrier dynamics in the polycrystalline films were strongly dependent on the probe wavelength. The

observed transient absorption signal varied from enhanced absorption with slow recovery at short wavelengths to enhanced transmission at long wavelength.

The thickness of the pc-Si film was found to have a large impact on the transient absorption signal due to multiple beam interference effects arising from the reflections from the air-silicon and silicon-substrate interfaces.

We have also found that the photoinduced carrier relaxation time in polycrystalline silicon films is carrier density dependent at densities larger than $1\times10^{20}cm^{-3}$ which correspond to large pump fluence values. Decreased carrier relaxation time at high carrier densities suggest that the Auger recombination process plays a primary role in the relaxation mechanism.

The study of transient photoinduced absorption in a nanocrystal silicon film revealed the presence of two different relaxation mechanisms in agreement with the observations in the work of Lioudakis *et al.*, 2007 and Klimov *et al.*, 1998. A fast relaxation with decay time ranging from (0.5 ± 0.1) ps for 600 nm probe wavelength to pulse width limited relaxation time for the 700 nm probe wavelength could be attributed to the relaxation of carrier to interface states. A slow relaxation process with decay time decreasing from (6.1 ± 0.9) ps for 600 nm probe to (4.8 ± 0.3) ps for 700 nm probe could be attributed to the relaxation of the carriers in the nanocrystal interior. Dependence of both the fast and slow decay times on the probe wavelength shows that different probe energies probe different energy states.

As in the case of the polycrystalline films, the investigation of pump fluence dependence of carrier relaxation in nanocrystal films demonstrated that the Auger recombination is the primary relaxation mechanism at high pump fluences.

While the investigation of the ultrafast transient absorption in nanostructured silicon films described in this thesis answered many questions about the photoexcited carrier dynamics, more detailed studies are needed for the complete understanding of the charge

carrier dynamics and relaxation processes in these materials. In order to proceed in this direction, several improvements to the experimental setup will be helpful.

First, the time resolution of the experimental setup needs to be improved to study the processes that occur on the times scales shorter than the resolution limit of the present setup. The straightforward way to achieve this is to minimize the effect of group velocity dispersion. This can by done by replacing the dispersive achromatic lenses by the reflective optical elements such as off axis parabolic mirrors.

The available probe wavelength range needs to be extended over the entire available white light continuum. To do so, the IR cutoff filter and the 435 nm filter used to block the fundamental and second harmonic light need to be replaced by the narrow band filters that will allow only the used probe wavelength to be detected by the photodetectors.

Adding a capability of simultaneously measuring transient reflectivity would be essential in order to get more accurate results for transient absorption and to be able to evaluate the contribution of the change in the refractive index, which cannot be obtained by measuring transient transmission alone.

Appendix A

A.1 Pulse Broadening and Relative Arrival Time Calculations

Dispersion Relation for water (Huibers 1997) and different optical materials between water and Kerr medium (Casix Catalouge, Schott Catalouge), and their thicknesses in our experiment are listed in table A.1.

Material	n(λ)	L (mm)
Water	$1.31279+15.762\lambda^{-1}+4382\lambda^{-2}+1.1455\times10^{6}\lambda^{-3}$	10
BK7	$(\frac{1.03961212\lambda^2}{\lambda^2-0.00600069867}+\frac{0.231792344\lambda^2}{\lambda^2-0.0200179144}+\frac{1.01046945\lambda^2}{\lambda^2-0.0103560653}+1)^{1/2}$	7
BaFN 10	$(\frac{1.5851495\lambda^2}{\lambda^2-0.00926681282}+\frac{0.143559385\lambda^2}{\lambda^2-0.0424489805}+\frac{1.08521269\lambda^2}{\lambda^2-105.613573}+1)^{1/2}$	7
SFL6	$(\frac{1.77931763\lambda^2}{\lambda^2-0.0133714182}+\frac{0.338149866\lambda^2}{\lambda^2-0.0617533621}+\frac{2.08734474\lambda^2}{\lambda^2-174.01759}+1)^{1/2}$	2
SF5	$(\frac{1.46141885\lambda^2}{\lambda^2-0.0111826126}+\frac{0.247713019\lambda^2}{\lambda^2-0.050594669}+\frac{0.949995832\lambda^2}{\lambda^2-112.041888}+1)^{1/2}$	2.5
Quartz	$(\frac{0.6961663\lambda^2}{\lambda^2-0.00467914826}+\frac{0.4079426\lambda^2}{\lambda^2-0.0135120631}+\frac{0.8974794\lambda^2}{\lambda^2-97.9340025}+1)^{1/2}$	1
Calcite	$(2.18438+\frac{0.0087309}{(\lambda^2-0.01018)}-0.002441\lambda^2)^{\frac{1}{2}}$	12

Table A.1: Dispersion relation and thicknesses for different optical elements between water cell and sample.

Example of calculation:

For water:

Using the dispersion relation in Table A.1, the refractive index, n, was calculated at different wavelengths. The derivative of the refractive index with respect to wavelength was obtained to be

$$\frac{dn}{d\lambda}=-15.762\lambda^{-2}+8764\lambda^{-3}-3.4365\times10^{6}\lambda^{-4} \qquad (A.1)$$

Using equation 2.8, v_g was calculated as shown in table A.2. From these values, N_g was calculated for the corresponding wavelengths and it was plotted in Fig. A.1.

λ(nm)	n	$v_g(\lambda)$ $(10^8 m/s^2)$	N_g	$\frac{dN_g}{d\lambda}$	Broadening (ps)	Relative Arrival Time (ps)
450	1.3388	2.2913	1.3093	0.00172	0.05746	0
480	1.3370	2.2882	1.3111	0.00154	0.05134	-0.789
520	1.3350	2.2854	1.3127	0.00134	0.04478	-0.361
580	1.3328	2.2830	1.3141	0.00087	0.02895	-0.555
600	1.3322	2.2825	1.3144	0.00075	0.02512	-0.606
630	1.3313	2.2819	1.3147	0.00057	0.01912	-0.673
650	1.3308	2.2817	1.3148	0.00057	0.01912	-0.712
680	1.3301	2.2814	1.3150	0.00057	0.01910	-0.764
700	1.3297	2.2813	1.3151	0.00049	0.01638	-0.795

Table A.2. Values used to calculate temporal broadening and relative arrival time.

The slope, $\frac{dN_g}{d\lambda}$, was calculated at each wavelength assuming the relation is linear for 10 nm bandwidth determined by the filter bandwidth. Using this result and equation 2.10, the temporal broadening of pulses, was calculated and plotted as a function of wavelength in Fig. A.2. The relative arrival time at each wavelength was calculated using equation 2.11 and plotted in Fig. A.3 as a function of wavelength.

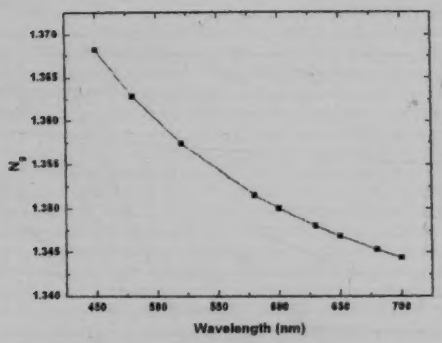

Figure A.1: Group index as a function of wavelength in 10 mm of water.

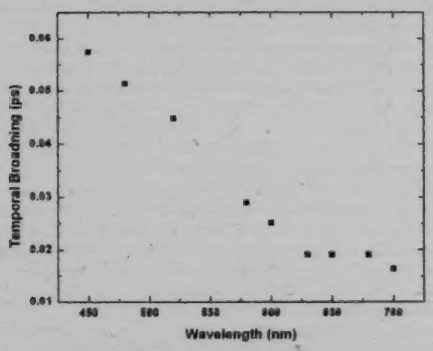

Figure A.2: Temporal broadening of pulses at different central wavelength in 10 mm of water.

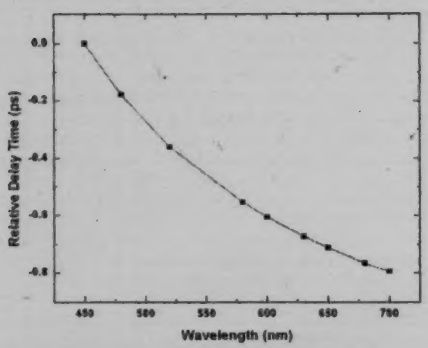

Figure A.3: Relative time delay of different pulses of different central wavelength propagating in 10 mm of water.

A.2 Filters bandwidth

It is stated in the manufacturer manual that the interference band pass filters provide 10 nm bandwidth around the specific wavelength. To check this, we measured the FWHM of the transmitted spectrums of the SC through these filters. An example is given for the 600 nm filter (Fig. A.4).

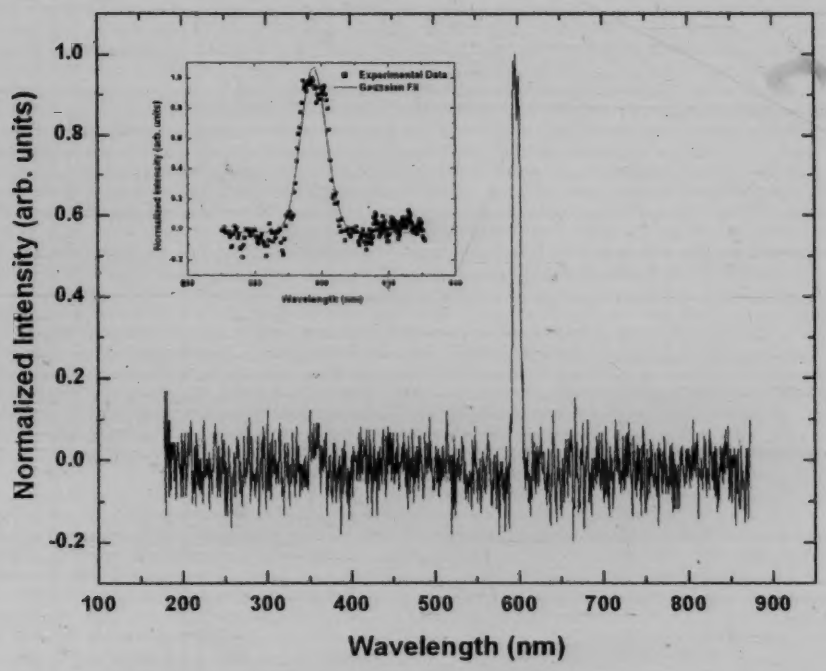

Figure A.4 Transmission through the 600 nm narrow bandwidth filter. Inset: A Gaussian fit results in FWHM = (8.9 ± 0.2) nm.

Appendix B

B.1 Experiment Consistency

It is important to ensure that signals we obtain are consistent and reproducible under the same experimental conditions. To check that, we consequently performed two scans. Each scan is the average of three individual scans with the same pump fluence and probe wavelength (Fig. B.1). The minimum signal is slightly varied due to the noise in the white light while the relaxation time constants are consistent within the experimental error.

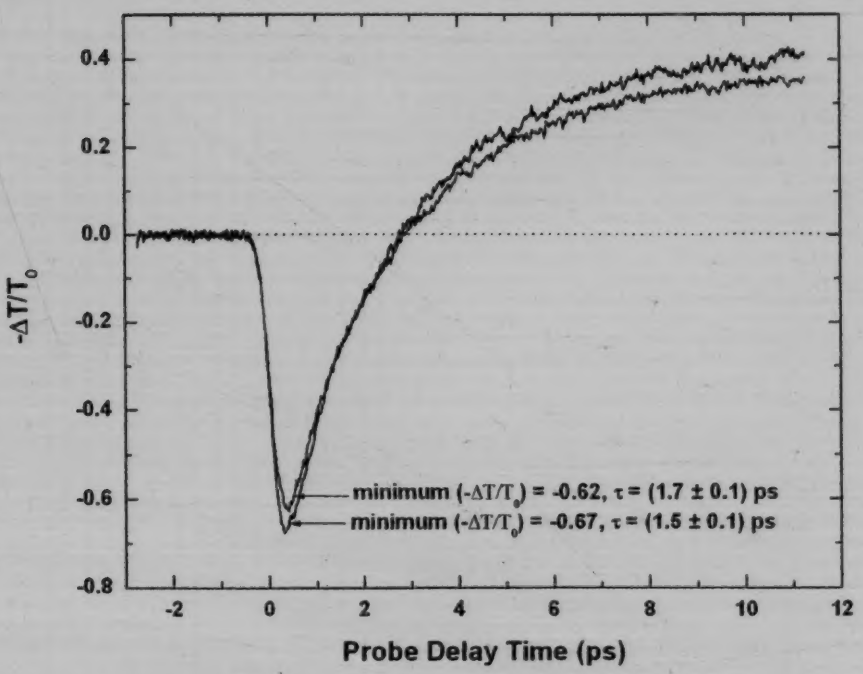

Figure B.1: Two transient absorption signals for two scans of the same pump fluence and probe wavelength.

B.2 Probe Fluence Dependence

The probe beam power must be low enough to not produce any change in the recorded transient absorption signal. To check whether there are effects of the probe fluence, we performed two scans with high and low probe fluences (Fig. B.2). We did not observe a probe fluence dependence.

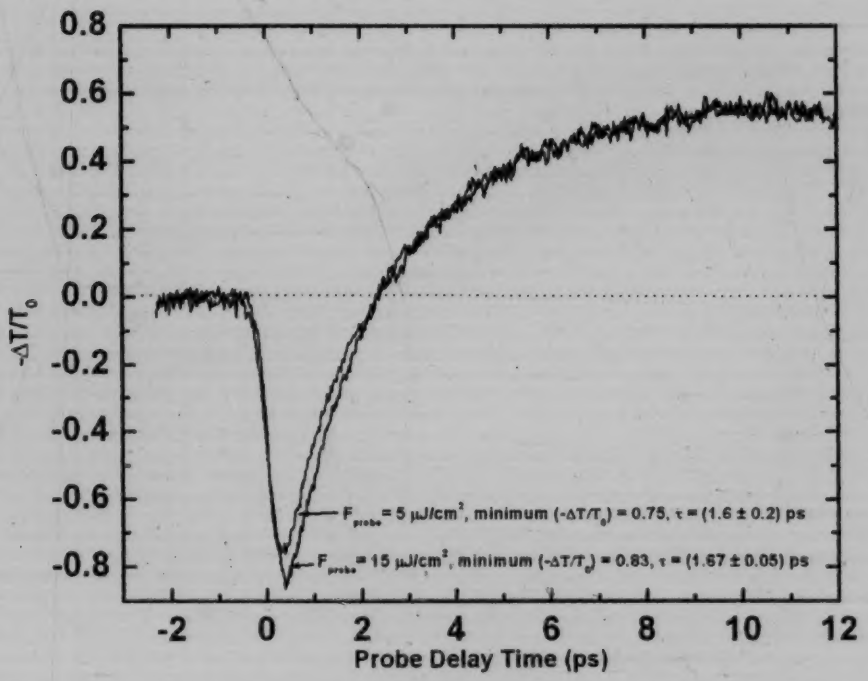

Figure B.2: Two different scans with different probe fluence.

B.3 Residual Signal

At very high pump fluences, it takes a long time for the sample to reach equilibrium state after photoexcitation. Thus, the probe pulse feels the modulation in the refractive index even when the probe pulse arrives at the sample before the pump pulse. This is due to the fact that the sample has not recovered completely after the preceding pump pulse. To check for such residual signal, we blocked the pump beam when the probe pulse arrives before the pump pulse. For low fluences, the signal was not affected and the base line remained at zero as expected. For high pump fluences, we observed a sight shift in the baseline signal indicating that the signal before the arrival of the next pump pulse is actually affected by the previous pump pulse. This residual signal was found to increase with increasing pump fluence.

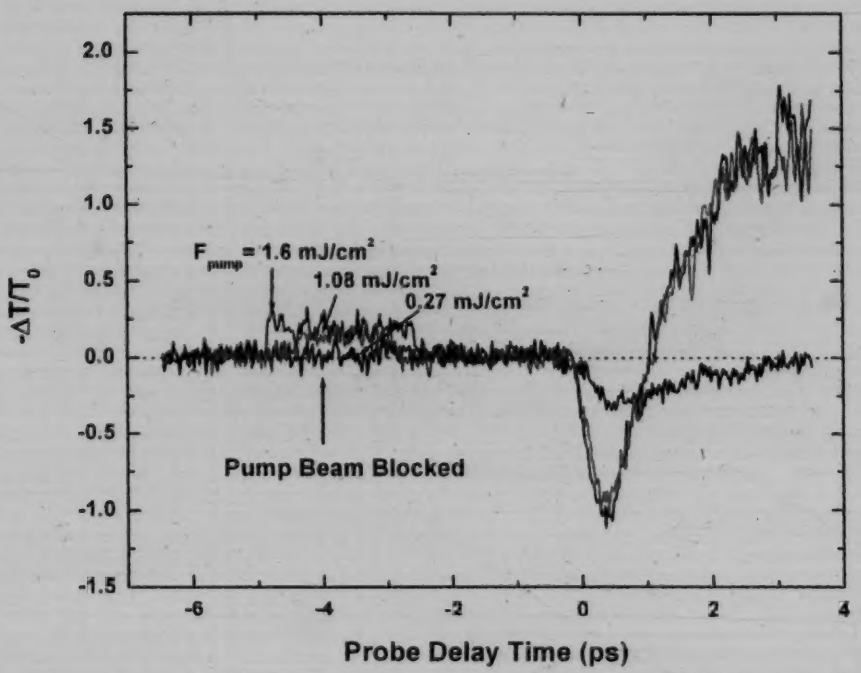

Figure B.3: Illustration of the effect of residual signal at different pump fluences.

B.4 Stimulated Emission Check

It is important to check whether the enhanced transmission in the signal observed in some polycrystalline silicon films is due to stimulated emission from the sample or not. This check is simply done by performing two scans with and without the sample in place. We divided the signal from the sample over the signal without the sample and found that the signal from the sample is always less than that without the sample. This indicates that there was no stimulated emission or gain from the sample.

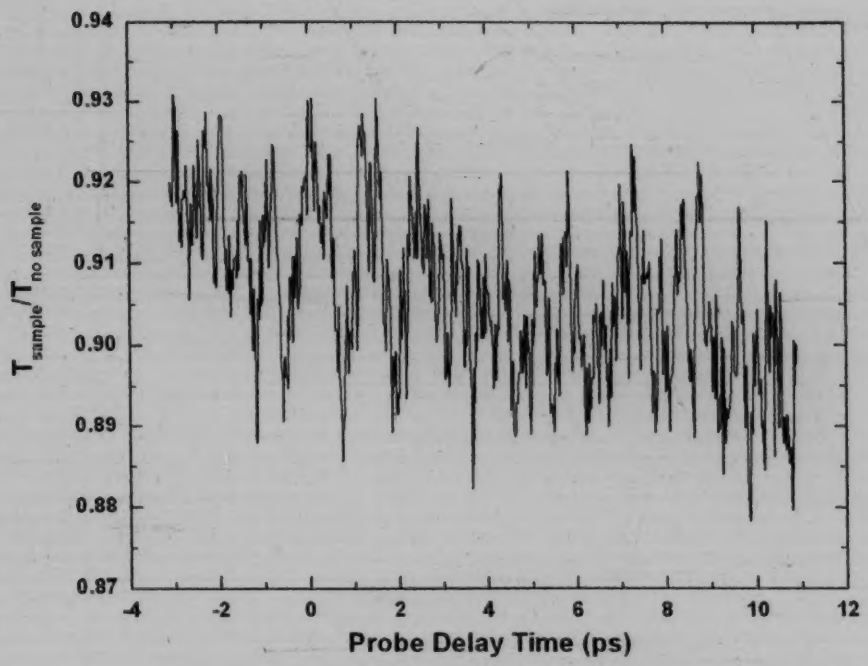

Figure B.4: Stimulated emission check for the 10 nm polycrystalline film and probe wavelength 630 nm.

References

Akozbek, N., M. Scalora, C.M. Bowden, and S. L. Chin, 2001
"White-light continuum generation and filamentation during the propagation of ultra-short laser pulses in air", Optics Communications, **191**, 353

Albrecht, H., P. Heist, J. Kleinschmidt, D. V. Lap, and T. Schroder, 1992,
"Measurement of ultraviolet femtosecond pulses using optica Kerr effect", Appl. Phys. B, **55**, 362.

Albrecht, H., P. Heist, J. Kleinschmidt, D. V. Lap, and T. Schroder, 1993,
"Single-shot measurement of femtosecond pulses using the optical Kerr effect", Meas. Sci. Technol., **4**, 492.

Alfano, R.R., 1986
"Frontier of femtosecond and picosecond optical measuring technique", Annals New York Academy of Science, **480**, 118.

Alfano, R.R., and S. L. Shapiro, 1970
"Observation of self-phase modulation and small filaments in crystals and glasses", Phys. Rev. Lett., **24**, 592.

Andor Technology catalogue, p. 150.

Antoncini, C.,
"Ultrashort laser pulses", (and references therein)

Behren, J., Y. Kostoulas, K. B. Ucer, P.M. Fauchet, 1996,
"The femtosecond optical response of porus, amorphous and crystalline silicon", Journal of Non-Crystalline Solids, **198-200**, 957.

Bread, M. C., K. P. Knutsen, P. Yu, J. M. Luther, Q. Song, W. K. Metzgar, R. J. Ellingson, and A. J. Nozik, 2007,
"Multiple exciton generation in colloidal silicon nanocrystals", Nano Letters, **7**, 2506.

Brodeur A., F.A. Ilkov, and S.L. Chin, 1996,
"Beam filamentation and the white light continuum divergence", Optics Communications **129**, 193.

Brodeur, A., and S. L. Chin, 1998
"Band-gap dependence of the ultrafast white light continuum", Phys. Rev. Lett., **80**, 4406.

Brodeur, A., and S. L. Chin, 1999
"Ultrafast white-light continuum generation and self-focusing in transparent condenced media", Opt. Soc. Am. B, **16**, 637

Canham, L. T, 1990,
"Silicon quantum wire array fabrication by electrochemical and chemical dissolution of wafers", Appl. Phys. Lett. 57, 1046.

Casix Catalouge.

Chavez, F.E.B., A.E. Martinez-Canton, C.J. Roman-Moreno, M. Garcia-Rocha, R. Ortega- Martinez, and A.A. Rodriguez-Rosales, 2005,
"Ultrashort laser pulses characterization by three optical methods: autocorrelation, optical interference and spectral analysis", Proc. Of SPIE, **5776**, 305.

Cooke, D. G., A. N. MacDonald, A. Hryciw, J. Wang, Q. Li, A. Meldrum, and F. A. Hegmann, 2006,
"Transient terahertz conductivity in photoexcited silicon nanocrystals films", Physical Review B, **73**, 193311.

Cooke, D. G., A. N. MacDonald, A. Hryciw, J. Wang, Q. Li, A. Meldrum, Q. Li and F. A. Hegmann, 2007,
"Ultrafast terahertz conductivity of photoexcited nonocrystalline silicon", J Mater Sci: Mater Electron, DOI 10.1007/s10854-007-9248-y.

Dahlstrom, L., and B. Kallberg, 1971,
"Third order correlation measurements of ultrashort light pulses", Optics Communications, **4**, 285.

Dharmadhikari, A.K., F.A. Rajgara, and D. Mathur, 2005,
"Systematic study of highly efficient white light generation in transparent materials using intense femtosecond laser pulses", Appl. Phys. B, **80**, 61.

Doany, F. E., D. Grischkowsky, and C. C. Chi, 1986,
"Carrier lifetime versus ion-implantation dose in silicon on sapphire", Appl. Phys. Lett., **50**, 460.

Doany, F. E., and D. Grischkowsky, 1987,
"Measurement of ultrashort hot-carrier relaxation in silicon by thin-film-enhanced, time resolved reflectivity", Appl. Phys. Lett., **52**, 1988.

Downer, M. C., and C. V. Shank, 1986,
"Ultrafast heating of silicon on sapphire by femtosecond optical pulses", Physical Review Letters, **56**, 761.

Dong-Hui, Q., L. Shi-Lin, Z. Lei, Y. Jain, W. Li, Y. Guo-Zhen, and W. Yu-Xiang, 2003,

"Experimental study of the chirp structure of the white-light continuum generation by femtosecond laser spectroscopy", Chin. Phys. Soc. **12**, 986.

Eaton, H., 1999,
"Studies on nonlinear femtosecond pulse propagation in bulk materials", Ph.D. Thesis.

Eckardt, R. C., and C. H. Lee, 1969
"Optical third harmonics measurements of subpicosecond light pulses", Appl. Phys. Lett., **15**, 425.

Edmund Catalouge.

Esser, A., K. Seibert, H. Kurz, G. N. Parsons, C. Wang, B.N. Davidson, G. Lucovsky, and R. J. Nemanich, 1990,
'Ultrafast recombination and trapping in amorphous silicon", Physical Review B, **41**, 2879.

Fauchet, P. M., D. Hulin, A. Migus, A. Antonetti, J. Kolodzey, and S. Wanger, 1986,
"Initial stage of trapping in a-Si:H observed by femtosecond spectroscopy", Phys. Rev. Lett., **57**, 2438.

Forst, M., M. Nagel, M. Awad, M. Wächter, T. Dekorsy, and H. Kurz, 2007,
"Coherent and ultrafast optoelectronics in III–V semiconductor compounds", phys. stat. sol. (b), **244**, 2971.

Gaponenko, S. V., 1998,
"Optical properties of semiconductors nanocrystals", Cambridge University Press.

Hadjisavvas, G., and P. C. Kelires, 2004,
"Structure and energetics of Si nanocrystals embedded in a-SiO_2", Phys. Rev. Lett., 93, 226104.

Ho, P. P., R. R. Alfano, 1978,
"Optical Kerr effect in liquids", Physical Review A, **20**, 2170.

Huibers, P. D. T., 1997,
"Models for the Wavelength Dependence of the Index of Refraction of Water", Applied Optics, **36**, 3785.

Huy, P. T., V. V. Thu, N. D. Chien, C. A. J. Ammerlaan, J. Weber, 2006,
"Structural and optical properties of Si-nanoclusters embedded in silicon dioxide", Physica B, **376-377**, 868.

Kasap, S.O., 2001,
"Optoelectronics and photonics", Prentice Hall.

Klimov, V., 2003,
"Nanocrystal quantum dots: from fundamental photophysics to multicolor lasing", Los Alamos Science, **28**, 214.

Klimov,V. I., Ch. J. Schwarz, D. W. McBranch, and C. W. White, 1998,
"Initial carrier relaxation dynamics in ion-implanted Si nanocrystals: Femtosecond transient absorption study", Appl. Phys. Lett., **73**, 2603.

Klimov,V. I., and D. W. McBranch, 1998,
"Femtosecond high-sensitivity, chirp free transient absorption spectroscopy using kilohertz lasers", Optics Letters, **23**, 277.

Lee, H. W. H., P. A. Thilelen, G. R. Delgado, S. M. Kauzlarich, B. R. Taylor, D. Mayeri, and C. S. Yang, 1998,
"Femtosecond pump-probe spectroscopy of quantum confined silicon and germainuim nanocrustals", IEEE, **98**, 200.

Lin, W. Z., R. W. Schoenlein, J.G. Fujmoto, and E. P. Ippen, 1988,
"Femtosecond Absorption Saturation Studies of Hot Carriers in GaAs and AlGaAs", IEEE Journal of Quantum Electronics, **24**, 267.

Lioudakis, E., A. Nassiopoulou, and A. Othonos, 2005,
"Ultrafast carrier dynamics in highly implanted and annealed polycrystalline silicon films", Journal of Physics, **10**, 263.

Lioudakis, E., A. Nassiopoulou, and A. Othonos, 2006,
"Ellipsometric analysis of ion-implanted polycrystalline silicon films before and after annealing', Thin Solid Films, 496, 253.

Lioudakis, E., A. Nassiopoulou, and A. Othonos, 2007,
"Ultrafast transient photoinduced absorption in silicon nanocrystals: coupling of oxygen related states to quantized sublevels", Appl. Phys. Lett., **90**, 171103.

Lioudakis, E., A. Nassiopoulou, A. Othonos, Ch. B. Lioutas, and N. Frangis, 2007,
"Influence of grain size on ultrafast carrier dynamics in thin nanocrystalline", Appl. Phys. Lett., **90**, 191114.

Lockwood, D. J., and L. Pavesi, 2004,
"Silicon funadamentals for photonics applications", Topics Appl. Phys., **94**, 1.

Luppi, M., and S. Ossicini, 2005,
"Ab initio study on oxidized silicon clusters and silicon nanocrystals embedded in SiO_2: beyond the quantum confinement effect", Physical Review B, **71**, 035340.

Maly, P., 2002

"Ultrafast laser spectroscopy of semiconductor nanocrystals", Czechoslovak Journal of Physics, **52**, 646.

Maly, P., K. Neudert, K. Zidek, M. Bittner, and F. Trojanek, 2007,
"Nonlinear spectroscopy and applications: time resolved nonlinear spectroscopy of silicon nanocrystals", Proc. Of SPIE, 6582, 65820N.

Marburger, J. H., 1975,
"Self-Focusing: Theory", Prog. Qant. Electr., **4**, 35.

Michelmann, K., T. Feurer, R. Frensler, and R. Saubery, 1996,
"Frequency resolved optical gating in the UV using the electronic Kerr effect", Appl. Phys. B., **63**, 485.

Midorikawa, K., H. Kawano, A. Suda, C. Nagura, and M. Obara, 2002,
" Polarization Properties of ultrafast whight-light continuum generated in condensed media", Appl. Phys. Lett. **80**, 923.

Mayers, K. E., Q. Wang, and S. L. Deheximer, 2001
"Ultrafsat carrier dynamics in nanocrystalline silicon", Physical Review B, **64**, 161309.

Nagura, C., A. Suda, H.Kawano, M. Obara, and K. Midorikawa, 2002,
"Generation and characterization of ultrafast white-light continuum in condensed media", Applied Optics, **41**, 3735.

Osaka Y, Tsunetomo K, Toyomura F, Myoren H, and Kohno K,
1992,
"Visible photoluminescence from Si microcrystals embedded in SiO2 glass films", Jpn J. Appl. Phys. 31 L365.

Othonos, A., 1998,
"Probing ultrafast and phonon dynamics in semiconductors", Journal of Applied Physics, **83**, 1789.

Othonos, A., and C. Christofides, 2002,
"Ultrafast dynamics in phosphorus silicon wafers: the effect of annealing", Physical Review B, **66**, 085206.

Palik, E. D., 1998,
"Handbook of optical constants of solids", Academic Press, p 564.

Pavesi, L., 2006,
"Silicon light emitters and amplifiers: state of art", Optical Interconnects, **4**.

Pavesi, L., L. Dal Negro, C. Mazzoleni, G. Franzo, and F. Priolo, 2000,

"Optical gain in silicon nanocrystals", Nature, **408**, 440.

Peatross, J., and A. Rundquist, 1998
"Temporal decorrelation of short laser pulses", Opt. Soc. Am. B, **15**, 216.

Rulliere, C., 1998
"Femtosecond Laser Pulses, Principles and Experiments", Spinger-Verlag, Heidelberg.

Schott Catalouge.

Shkrob, A., R. A. Crowell, 1998,
"Ultrafast change recombination in undoped amorphous hydrogenated silicon", Physica Review B, **57**, 12207.

Slepkov, A. D., 2002,
"Third-order nonlinearities of novel iso-polydiacetylenes studied by a differential optical Kerr effect detection technique", MSc Thesis.

Slepkov, A. D., 2006,
"Ultrafast third-order optical nonlinearities of conjugated organic molecules", Ph.D Thesis.

Steinmeyer, G., D. H. Sutter, L. Gallmann, N. Matuschek, and U. Keller, 1999
"Frontier in ultrafast pulse generation: pushing the limits in linear and nonlinear optics" Science, **286**, 1507.

Takeda, J., K. Nakajima, and S. Kurita, 2000,
"Time resolved luminescence spectroscopy by the optical Kerr-gate method applicable to ultrafast relaxation processes", Phys. Rev. B., **62**, 10 083.

Tanaka, T., A. Harata, and T. Sawada, 1997,
"Subpicosecond surface restricted carrier and thermal dynamics by transient reflectivity measurements", J. Appl. Phys., **82**, 4033.

Tanguy, C., D. Hulin, A. Mourchid, P. M. Fauchet, and S. Wanger, 1988,
"Free-carrier and temperature effects in amorphous silicon thin films", Appl. Phys. Lett., **53**, 880.

Thorlabs Catalogue, Volume 18.

Tripathy, S., R. K. Soni, S. K. Ghoshal, and K. P. Jain, 1998,
"Optical properties of nano-silicon", Bull Mater. Sci., **24**, 285.

Walmsley, I., L. Waxer, and C. Dorrer, 2001,

"The role of dispersion in ultrafast optics", Review of Scientific Instruments", **72**, 1.

Weber, H. P., and R Dandliker, 1968,
"Methods for measuring the shape asymmetry of picosecond light pulses", Physics Letters, **28A**, 77.

Wu, F., and J. Z. Zhang, 2004,
"Charge carrier dynamics of nanoparticles", Dekker Encyclopedia of Nanoscience and Nanotechnology, 667.

Xing Q., K. M. Yoo, and R. R. Alfano, 1993,
"Conical emission by four-photon parametric generation by using femtosecond laser pulses", Applied Optics, **32**, 2087.

Yamaguchi, S., and H. Hamaguchi, 1995,
"Convenient method of measuring the chirp structure of femtosecond wight-light continuum pulses", Applied Spectroscopy, **49**, 1513.

Yuan-Dong, Q., W. Dan-Ling, W. Shu-Feng, and G. Qi-Huang, 2000,
"Spectral and temporal properties of femtosecond white-light continuum generated in H_2O", Chin. Phys. Lett., **18**, 390.